2005

Modeling of dry-casting and non-solvent vapor induced phase separation

Yuen-Lai Yip
Lehigh University

Yip, Yuen-Lai

Modeling of Dry-casting and Non-solvent Vapor Induced Phase Separation

May 2005

Modeling of Dry-casting and Non-solvent Vapor Induced Phase Separation

By

Yuen-Lai Yip

A Thesis

Presented to the Graduate and Research Committee

of Lehigh University

in Candidacy for the Degree of Master of Science

in

Chemical Engineering

Lehigh University

May 2005

Certificate of Approval

This thesis is accepted and approved in partial fulfillment of the requirements for the degree of Master of Science in chemical engineering.

19 April 05

Date

Thesis Advisor

Chairperson of Department

To Mom and Dad

Acknowledgments

I would like to thank God for His blessings, love and grace. His constant spiritual support is always my motivation in performing the best for His glory. I also would like to express my sincere gratitude to my parents for their efforts in providing me a good learning environment since I was born.

I would like to thank Professor A. J. McHugh for his guidance through the course of this work. His confidence and encouragement during the time when I had many problems with my computational results was particularly appreciated. I also thank the past members of the McHugh group for their valuable notebooks and computer programs, and their willingness to help through e-mails.

Finally, I would like to offer a special thanks to Mr. Decheng Ma for early development of the mathematical model and the many discussions we have had. I also would like to acknowledge Professor W. E. Schiesser for his advice on the numerical algorithm.

Financial support from Lehigh University's Byllesby Fellowship and the Rossin Professorship are gratefully acknowledged.

Table of Contents

List of Figures

List of Tables

Abstract

A model is developed for both dry-casting and nonsolvent vapor induced phase separation (VIPS). The model incorporates coupled heat and mass transfer, ternary diffusion as well as moving boundary at the polymer solution/air interface. It can predict mass transfer paths, composition profiles, film temperature, and thickness for evaporation of both solvent and nonsolvent from a ternary polymer/solvent/nonsolvent system or evaporation of solvent from a binary polymer/solvent system under an atmosphere containing the nonsolvent vapor. Four systems used for simulations are cellulose acetate(CA)/acetone/water, poly(vinylidene fluoride)(PVDF)/dimethylformamide (DMF)/water, polysulfone(PS)/N-methyl-2-pyrolidone(NMP)/water and poly(etherimide)(PEI)/ NMP/water. By superposing mass transfer paths onto the ternary phase diagram, a number of detailed morphological features can be predicted. The effects of different input parameters like initial nonsolvent/polymer concentration, initial film thickness, evaporation temperature, air velocity and relative humidity are investigated. A critical humidity is needed to induce phase separation in VIPS and it is closely related to the nature of the homogeneous region of the ternary phase diagram. The role of diffusion formalism on the morphological predictions is also illustrated to show the accuracy of the multicomponent diffusion theory.

Chapter 1

Introduction

Phase inversion is a process in which an initially homogeneous polymer solution thermodynamically becomes unstable due to external effects and phase separates into a continuous polymer-rich phase that surrounds dispersed polymer-lean droplets. This process is widely used in the fabrication of polymeric membranes for a variety of applications. Phase inversion of polymer solutions can be induced by any one or combination of the following driving forces: temperature (thermal induced phase separation) [1-3], nonsolvent (nonsolvent induced phase separation/wet-casting) [4], evaporation (dry-casting) [5-10], water vapor (nonsolvent vapor induced phase separation) [11-15], reaction [16] and shear stress (shear-induced phase separation) [17]. There have been extensive studies on the kinetics of phase separation for different polymer systems aiming at prediction and control of the morphology of the final membrane structure. In particular, nonsolvent induced phase separation and thermally induced phase separation have been studied in detail. Since phase inversion is a multiple-parameter process, a large variety of membrane structures ranging from symmetric to asymmetric can result. In order to optimize the polymer formulation and operating conditions to achieve the desired membrane morphology efficiently without trial-and-error experimentation, a reliable mathematical model which can capture the membrane formation kinetics is needed.

There are relatively few modeling works in the literature related to dry-casting or nonsolvent vapor induced phase separation although they have some advantages especially in polymer coating compared to other phase inversion techniques. A ternary polymer solution containing polymer, solvent and nonsolvent is dried under a humid/dry atmosphere in dry-casting whereas a binary polymer solution containing only polymer and solvent is dried under an atmosphere containing the nonsolvent vapor (usually water) in VIPS. A schematic of dry-casting is shown in Figure 1.1. A casting solution containing polymer, solvent and nonsolvent is placed in a dry/humid atmosphere. The evaporation of solvent and nonsolvent from the initially homogeneous single-phase polymer solution drives the ternary mixture entering the binodal region [4] which causes the solution to separate into two phases by liquid-liquid de-mixing. Solidification then follows in which the polymer from the polymer-rich phase precipitates to form a solid matrix which envelopes the solvent-rich phase. The solvent-rich phase can be a collection of interconnected droplets or individual droplets dispersed in the polymer-rich phase. In VIPS, phase separation is entirely driven by the relative humidity in the air. When a sufficient amount of water (acts as nonsolvent) has diffused into the polymer solution from the air, the initial binary mixture of the polymer and solvent enters the binodal region and phase separates.

The morphology formed upon phase separation is a critical factor in determining the performance of the final phase inverted structure. In the case of polymer depots for injectable drug delivery, it determines the drug release characteristics of the encapsulated drug [18]. Two possible morphologies like the finger-like and sponge-like structures are shown Figures 1.2a and 1.2b.

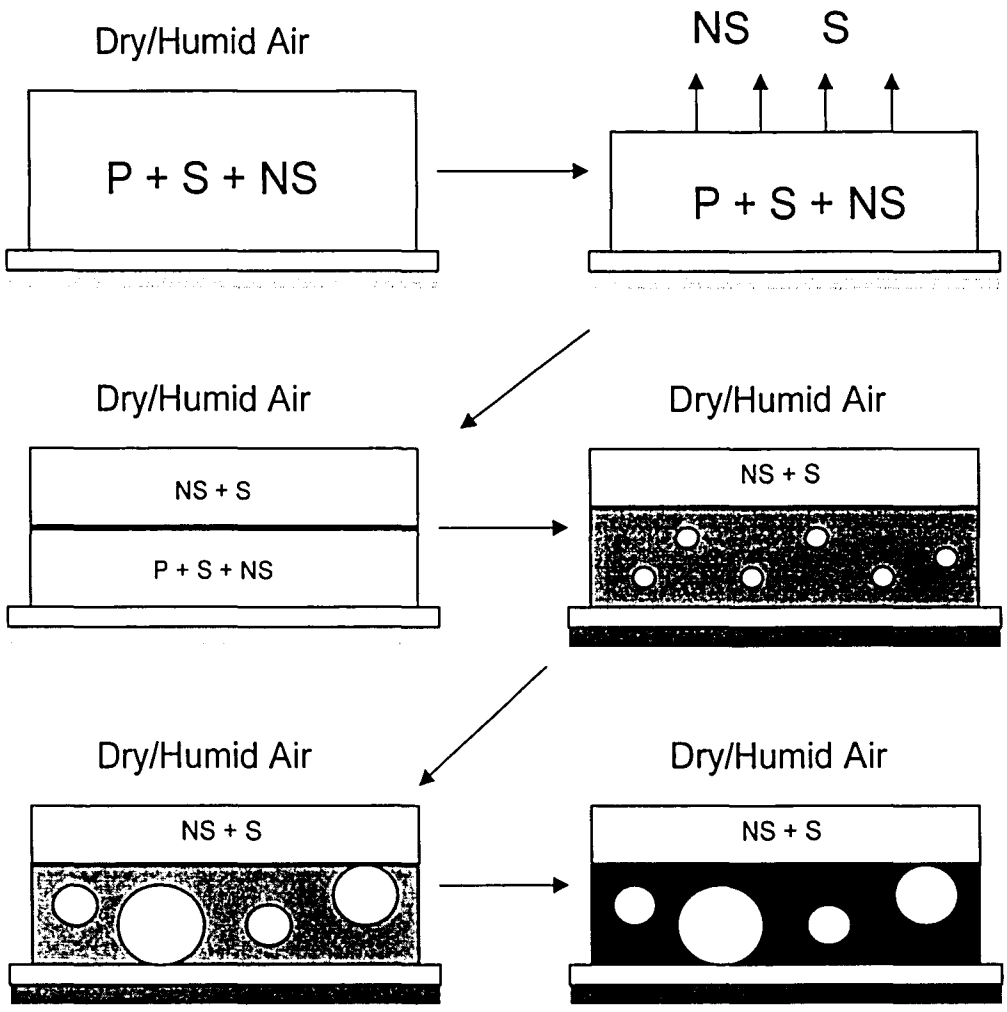

Figure 1.1: Schematic of dry-casting.

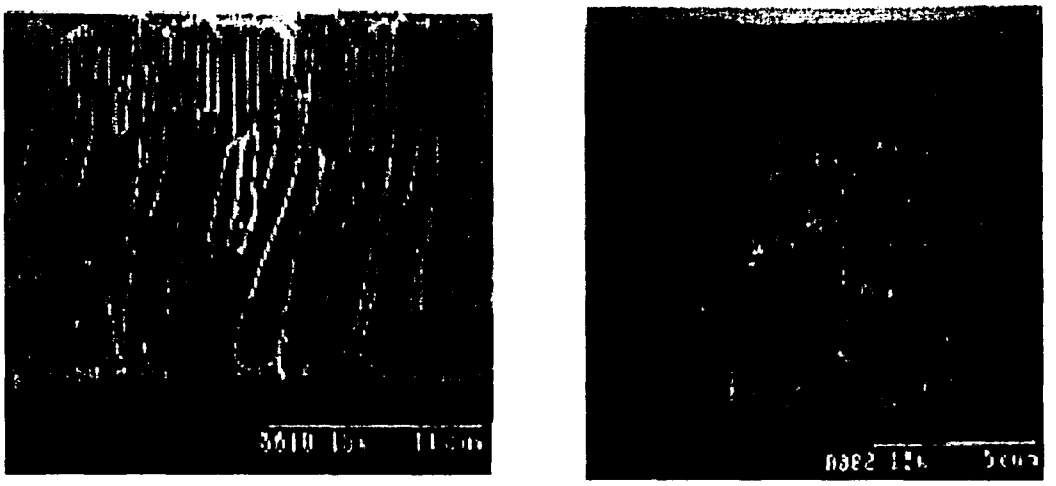

Figure 1.2: Morphologies formed upon phase separation (a) Finger-like (b) Sponge-like (from reference [19]).

Models related to both processes have been developed for evaporative casting of dense films from binary polymer solutions. Early models [20-23] neglected the temperature change inside the film and utilized self diffusion coefficients instead of mutual diffusion coefficients. The first ternary evaporative casting model that incorporated coupled heat and mass transfer was derived by Shojaie et al. [5]. In their model, mass transfer of solvent and nonsolvent were analyzed by incorporating excess volume of mixing effects. Film shrinkage was considered due to both excess volume of mixing and evaporative solvent and nonsolvent loss, and temperature profiles within the film were predicted by solving the unsteady-state heat transfer equation. They utilized a simplified form of Bearman's friction-based theory in which self diffusion coefficients are related to ternary mutual diffusivities through friction coefficients and self diffusion coefficients were predicted from Fujita's free volume theory. In a subsequent paper, Shojaie et al. [6] validated the dry-casting model by comparing measurements of total

mass loss and temperature with the model predictions, and commented that the model predictions were quite sensitive to the mass and heat transfer coefficients. The effects of initial composition and casting thickness on the final membrane morphology were also investigated, and all the simulations were based on the cellulose acetate/acetone/water system. Matsuyama et al. [7-8, 11-12] studied membrane formation and morphological development by both dry-casting and VIPS processes experimentally. In their VIPS model for the poly(vinylidene fluoride)/dimethyl formamide/water system, assumptions of isothermal process and quasi binary system were made. The main and cross diffusion coefficients for the solvent were replaced by a mutual diffusion coefficient estimated using Vrentas-Duda free volume theory. In a recent paper, Altinkaya et al. [9] modeled asymmetric membrane formation by dry-casting. Their model took into account film shrinkage, evaporative cooling, coupled heat and mass transfer and utilized the friction-based diffusion model proposed by Alsoy and Duda coupled with self diffusion coefficients predicted from Vrentas-Duda's free volume theory. The use of constant mass and heat transfer coefficients as input parameters is critical since the model predictions could be quite sensitive to the mass and heat transfer coefficients which are two of the controlling parameters in membrane casting. Altinkaya et al. investigated the effect of initial composition in casting solution, initial film thickness, evaporation temperature, relative humidity, air velocity and diffusion formalism on the final membrane morphology, and cellulose acetate/acetone/water was chosen as the model system [10]. It was shown that the predictions of this model were in good agreement with morphological studies.

Phase inversion is strongly influenced by relative humidity in nonsolvent vapor induced phase separation. There have been a few morphological studies relating between mass transfer and relative humidity in VIPS for different systems like poly(vinylidene fluoride)/dimethyl formamide/water [11], polysulfone/N-methyl-2-pyrolidone/water [13-14], poly(etherimide)/ N-methyl-2-pyrolidone/water [15]. However, there is no complete model that considers coupled heat and mass transfer for predicting the critical humidity for phase separation in VIPS.

In this thesis, a model with adjustable parameters that allows the prediction of evaporation of solvent and/or nonsolvent from the film and diffusion of nonsolvent into the film from the atmosphere is developed. This can apply to both dry-casting and nonsolvent vapor induced phase separation for different systems. Four different systems used for simulations are CA/acetone/water, PVDF/NMP/water, PSF/NMP/water and PEI/NMP/water. The primary purpose of this thesis is to extend the dry-cast model to VIPS processes and to see the difference in morphological predictions for the two processes. We attempt to show the ability of the model in capturing all important thermodynamic and kinetic aspects. The thesis is organized as follows: Chapter 2 contains the thermodynamics and mass transfer dynamics of polymer-solvent-nonsolvent system during evaporation. Chapter 3 contains the mathematical description of the model and the numerical method. Chapter 4 covers the computational results of different input parameters for dry-casting and Chapter 5 covers the computational results of different input parameters for VIPS. Finally, Chapter 6 has the conclusions and discussions.

Chapter 2

Background

In order to develop a mathematical model for dry-casting and nonsolvent vapor phase separation, it is essential to understand the thermodynamics and mass transfer dynamics of the polymer-solvent-nonsolvent system during evaporation.

2.1 Thermodynamics of polymer-solvent-nonsolvent systems

Yilmaz and McHugh [24] have extended the binary form of Flory-Huggins theory to ternary systems in order to construct ternary phase diagrams, which describe the phase behavior of polymer-solvent-nonsolvent systems. According to their analysis, the Gibbs free energy of mixing for ternary systems can be expressed in terms of three concentration-dependent binary interaction parameters as:

$$\frac{\Delta G_M}{RT} = n_1 \ln \phi_1 + n_2 \ln \phi_2 + n_3 \ln \phi_3 + g_{12}(u_2) n_1 \phi_2 + g_{13}(\phi_3) n_1 \phi_3 + g_{23}(\phi_3) n_2 \phi_3 \qquad (2.1.1)$$

In Equation (2.1.1), n_i is mole of i, ϕ_i is volume fraction of $i, u_2 = \phi_2 /(\phi_1 + \phi_2)$, and g_{ij}'s are the binary interaction parameters. The subscripts refer to nonsolvent (1), solvent (2), and polymer (3).

The chemical potential of each component can be evaluated as follows:

$$\frac{\Delta\mu_i}{RT} = \frac{\partial}{\partial n_i}\left(\frac{\Delta G_M}{RT}\right)_{n_j, j\neq i} \tag{2.1.2}$$

where μ_i is the chemical potential of each of the components.

The expressions for the derivatives of the chemical potentials are given below [4]:

$$\frac{\partial}{\partial\phi_1}\frac{\Delta\mu_1}{RT} = \frac{1}{\phi_1} - 1 + \frac{v_1}{v_3} + \phi_2\left(\frac{v_1}{v_2}g_{23} - g_{12}\right) - (\phi_2 + 2\phi_3)g_{13} + (\phi_1 - 2u_2)u_2{}^2\frac{dg_{12}}{du_2}$$

$$+ 3\frac{v_1}{v_2}\phi_2\phi_3\frac{dg_{23}}{d\phi_3} + u_1u_2{}^3\frac{d^2g_{12}}{du_2{}^2} + \frac{v_1}{v_2}\phi_2\phi_3{}^2\frac{d^2g_{23}}{d\phi_3{}^2} \tag{2.1.3}$$

$$\frac{\partial}{\partial\phi_2}\frac{\Delta\mu_1}{RT} = -\frac{v_1}{v_2} + \frac{v_1}{v_3} + (\phi_2 + \phi_3)(g_{12} - g_{13}) + \frac{v_1}{v_2}(\phi_2 - \phi_3)g_{23} + u_1u_2(u_2 - u_1 - \phi_1)\frac{dg_{12}}{dh_2}$$

$$+ \frac{v_1}{v_2}\phi_3(3\phi_2 - \phi_3)\frac{dg_{23}}{d\phi_3} - u_1{}^2u_2{}^2\frac{d^2g_{12}}{du_2{}^2} + \frac{v_1}{v_2}\phi_2\phi_3{}^2\frac{d^2g_{23}}{d\phi_3{}^2} \tag{2.1.4}$$

$$\frac{\partial}{\partial\phi_1}\frac{\Delta\mu_2}{RT} = -\frac{v_2}{v_1} + \frac{v_2}{v_3} + (\phi_1 + \phi_3)\left(\frac{v_2}{v_1}g_{12} - g_{23}\right) + \frac{v_2}{v_1}u_1u_2(\phi_2 + u_2 - u_1)\frac{dg_{12}}{du_2}$$

$$+ \phi_3(3\phi_2 - 1)\frac{dg_{23}}{d\phi_3} - \frac{v_2}{v_1}u_1{}^2u_2{}^2\frac{d^2g_{12}}{du_2{}^2} + \phi_2\phi_3{}^2\frac{d^2g_{23}}{d\phi_3{}^2} \tag{2.1.5}$$

$$\frac{\partial}{\partial\phi_2}\frac{\Delta\mu_2}{RT} = \frac{1}{\phi_2} - 1 + \frac{v_2}{v_3} + \frac{v_2}{v_1}\phi_1(g_{13} - g_{12}) - (\phi_1 + 2\phi_3)g_{23} + \frac{v_2}{v_1}u_1{}^2(2u_1 - \phi_2)\frac{dg_{12}}{du_2}$$

$$+ \phi_3(4\phi_2 + \phi_1 - 2)\frac{dg_{23}}{d\phi_3} + \frac{v_2}{v_1}u_1{}^3u_2\frac{d^2g_{12}}{du_2{}^2} + \phi_2\phi_3{}^2\frac{d^2g_{23}}{d\phi_3{}^2} \tag{2.1.6}$$

The important aspects of the phase diagram are (1) the binodal curve (2) the spinodal curve (3) the solidification curve. The binodal curve is a locus of points for which the system consists of two phases in equilibrium with each other and hence the chemical

potential of each component is equal in both phases. Mathematically, it can be written as

$$\Delta\mu_{i,A} = \Delta\mu_{i,B} \qquad i = 1, 2, 3 \tag{2.1.7}$$

where subscripts A and B refer to the polymer-rich and polymer-lean phases, respectively. The spinodal region is where concentration fluctuations grow in magnitude and lead to phase separation called spinodal decomposition. The spinodal curve is evaluated from the following relation for ternary systems:

$$G_{23}G_{33} = (G_{23})^2 \tag{2.1.8}$$

In Equation (2.1.8), G_{ij} are defined as follows:

$$G_{ij} = \left(\frac{\partial^2 \overline{\Delta G_M}}{\partial\phi_i \partial\phi_j} \right) v_1 \tag{2.1.9}$$

where v_1 is the molar volume of the nonsolvent.

Solidification occurs due to one or more of the following phenomena (1) gelation (2) glass transition or (3) crystallization.

Ternary phase diagrams are useful in allowing a quick description of the phase transitions that are possible during the evaporation step.

2.2 Determination of Thermodynamics Parameters

Nonsolvent-Solvent Interaction Parameter

The nonsolvent-solvent interaction parameter can be determined by the following equation:

$$g_{12} = \frac{1}{x_1 \phi_2}\left(x_1 \ln\left(\frac{x_1}{\phi_1}\right) + x_2 \ln\left(\frac{x_2}{\phi_2}\right) + \frac{\Delta G^E}{RT}\right) \tag{2.2.1}$$

ΔG^E is the excess free energy of mixing and it can be evaluated by:

$$\frac{\Delta G^E}{RT} = x_1 \ln \gamma_1 + x_2 \ln \gamma_2 \tag{2.2.2}$$

where γ_1 and γ_2 can be evaluated from the vapor liquid equilibrium data or the UNIFAC model [25].

Polymer-Solvent Interaction Parameter

There are a number of techniques to estimate the polymer-solvent interaction parameter and they include osmotic pressure measurements, vapor pressure measurements, gas chromatography and light scattering. Vapor pressure measurements are the most commonly used method and g_{23} is given by:

$$g_{23} = \frac{\ln\left(\frac{p_2}{(1-p_2^{\,0})\phi_3}\right) - \phi_3\left(1 - \frac{v_2}{v_3}\right)}{\phi_3^{\,2}} \tag{2.2.3}$$

where p_2 is the vapor pressure of the solvent in equilibrium with a polymer solution with a volume fraction of polymer ϕ_3. $p_2^{\,0}$ is the vapor pressure of pure solvent, v_2 and v_3 are the molar volumes of the solvent and polymer respectively.

Nonsolvent-polymer interaction parameter

The nonsolvent-polymer interaction parameter is usually measured using swelling experiments. The polymer is casted as a film and soaked in the nonsolvent until equilibrium is attained. If the equilibrium uptake of nonsolvent is small, the Flory-Rehner theory can be used to estimate g_{13} [26].

$$g_{13} = -\frac{\left(\ln\left(1-\phi_{3,eq}\right)+\phi_{3,eq}\right)}{\phi_{3,eq}^{\ 2}} \tag{2.2.4}$$

where $\phi_{3,eq}$ is the volume fraction of the polymer at equilibrium in the swollen polymer film.

2.3 Mass Transfer Dynamics in Casting Solutions

A detailed understanding of the morphology development that occurs under a given set of processing conditions requires knowledge of the location of the solution composition on the ternary phase diagram as well as the composition profiles in the film during the evaporation process. Tsay and McHugh [23] developed an isothermal evaporation model applicable to binary polymer-solvent systems prior to the nonsolvent quench in the wet cast process. The basic assumptions of their model are: (1) no volume change on mixing; (2) ideal gas behavior on air side; (3) gas-liquid equilibrium at the air-film interface. Following these assumptions, the governing diffusion equation, initial condition and boundary conditions can be written as follows:

$$\frac{\partial \rho_2}{\partial t} = \frac{\partial}{\partial z}\left(D\frac{\partial \rho_2}{\partial z}\right) \tag{2.3.1}$$

$$\rho_2 = \rho_{20} \tag{2.3.2}$$

$$\frac{\partial \rho_2}{\partial z} = 0 \qquad \text{at } z = 0 \tag{2.3.3}$$

$$\frac{d}{dt}\left(\int_0^{l(t)} \rho_2 dz \right) = -k(\rho_{2gl} - \rho_{2g\infty}) \qquad \text{at } z = l(t) \tag{2.3.4}$$

where ρ_i, D, t, and z represent the mass density of component i, binary diffusion coefficient, time and position, respectively.

Equations (2.3.1)-(2.3.4) can be modified to ternary systems for evaporative casting. Mass transfer paths that describe solution-gas interface composition and variation with time can be calculated from the model. Thus, by superposing mass transfer paths onto the ternary phase diagram, a number of detailed morphological features can be predicted. For example, Tsay and McHugh [27] used the ternary phase diagram shown in Figure 2.3.1 as an aid to postulate mechanistic changes and resultant film morphology transitions for their wet cast process with evaporation and quench. As initial polymer solution compositions between points A and B undergo a glass transition, a homogeneous and dense structure is formed. For initial compositions between points B and C, nucleation and growth followed by glass transition is the expected mechanism and it leads to a skin structure comprised of polymer-lean droplets trapped in a polymer-rich, glassy region and a finger-type substructure. A third possibility corresponds to initial compositions between points C and D. The expected phase separation dynamics for this case is spinodal decomposition, which eventually leads to a glass transition. The resulting skin structure contains a significant polymer-lean phase surrounded by a glassy, polymer-rich phase at the surface, while the rest consists of fingers. Similar analysis can be employed for the phase separation process when solutions are allowed to dry instead of being quenched into a coagulation bath.

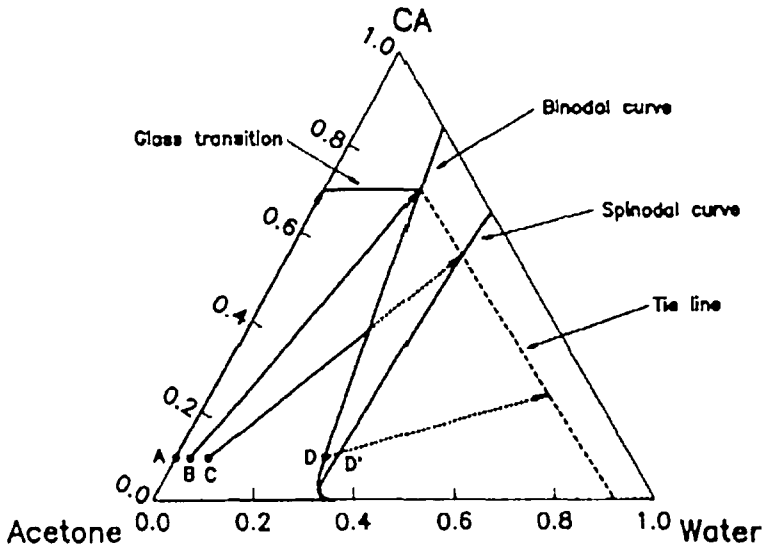

Figure 2.3.1. Ternary phase diagram and desolvation lines for cellulose/acetone/water system. (from reference [27])

Chapter 3

The Model and the Numerical Method

The objective of this model is to predict the phase inversion kinetics and film morphology for evaporation of both solvent and nonsolvent from a ternary polymer/solvent/nonsolvent system or evaporation of solvent from a binary polymer/solvent system under an atmosphere containing the nonsolvent vapor. This chapter describes the mathematical formulation of the model, estimation of the parameters used in the model and the numerical method.

3.1 Mass and Heat Transfer Model

The non-isothermal evaporation model for the polymer-solvent-nonsolvent ternary system is based on the binary model developed by Tsay and McHugh [23]. The geometry is illustrated in Figure 3.1.1. This model incorporates the concept that nonsolvent diffusion can occur from a humid environment to binary polymer casting solution during the evaporation process. The basic assumptions are (1) One-dimensional diffusion, (2) No polymer transfer to the air side, (3) No heat transfer from the casting substrate, (4) Constant partial specific volume, (5) Uniform temperature through the solution and substrate, (6) No volume change on mixing, (7) Ideal gas behavior at air side,

and (8) Gas-liquid equilibrium at the air-film interface. Following these assumptions, the governing diffusion equations for the general ternary system can be written as follows:

$$\frac{\partial \rho_i}{\partial t} = \frac{\partial j_i^v}{\partial z} \qquad i = 1, 2, 3 \tag{3.1.1}$$

where ρ_i and j_i^v are the density and mass flux of component i with respect to the volume-average velocity, respectively. Subscripts refer to nonsolvent (1), solvent (2), and polymer (3), respectively. The definition of ρ_i is given by

$$\rho_i = \frac{\phi_i}{\hat{V}_i} \tag{3.1.2}$$

where $\hat{V}_i$ and ϕ_i are the partial specific volume and volume fraction of component i. The diffusive fluxes, j_i^v can be written in terms of the ternary diffusion coefficients, D_{ij}, as follows:

$$j_i^v = -\sum_{j=1}^{3} D_{ij} \frac{\partial \rho_j}{\partial z} \tag{3.1.3}$$

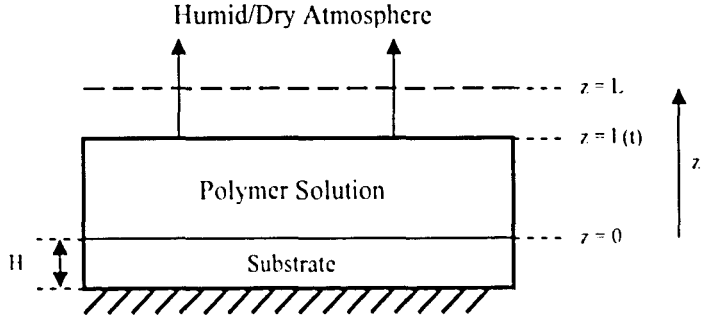

Figure 3.1.1: Schematic of the dry-cast model. The initial film interface is at L, while l(t) represents an arbitrary location at time t.

In order to facilitate numerical treatment of the moving interface, *l(t)*, the following coordinate transformations are used:

$$\eta = \frac{z}{l(t)} \quad for\ 0 \le z \le l(t) \tag{3.1.4}$$

$$t^{*} = \frac{D_0 t}{L^2} \tag{3.1.5}$$

where D_0 is characteristic diffusivity and L is initial film thickness.

Consequently, the final set of dimensionless diffusion equations for nonsolvent and solvent becomes the following:

$$\frac{\partial \phi_1}{\partial t^{*}} = \frac{\eta}{l}\frac{dl}{dt}\frac{\partial \phi_1}{\partial \eta} + \frac{1}{l^2}\frac{\partial}{\partial \eta}\left(\frac{D_{11}}{D_0}\frac{\partial \phi_1}{\partial \eta} + \frac{\hat{V}_1}{\hat{V}_2}\frac{D_{12}}{D_0}\frac{\partial \phi_2}{\partial \eta}\right) \tag{3.1.6}$$

$$\frac{\partial \phi_2}{\partial t^{*}} = \frac{\eta}{l}\frac{dl}{dt}\frac{\partial \phi_2}{\partial \eta} + \frac{1}{l^2}\frac{\partial}{\partial \eta}\left(\frac{\hat{V}_2}{\hat{V}_1}\frac{D_{21}}{D_0}\frac{\partial \phi_1}{\partial \eta} + \frac{D_{22}}{D_0}\frac{\partial \phi_2}{\partial \eta}\right) \tag{3.1.7}$$

Temperature is assumed to be uniform throughout the polymer solution, which agrees with Shojaie's prediction of flat temperature profile throughout the membrane formation [5]. Heat transfer can then be determined by a lumped parameter approach [9] and the time dependence of the temperature is given by the following equation assuming no heat transfer in the substrate:

$$\frac{dT}{dt} = -\left[\frac{h^G(T - T^G) + \frac{k_1}{\hat{V}_{1g}}(y_{1gl} - y_{1gv})\Delta\hat{H}_{v1} + \frac{k_2}{\hat{V}_{2g}}(y_{2gl} - y_{2gv})\Delta\hat{H}_{v2}}{\rho^p \hat{C}_p^p z(t) + \rho^s \hat{C}_p^s H}\right] \tag{3.1.8}$$

where the subscripts *g*, *t* and ∞ refer to gas phase side, air-film interface, and position away from the interface, and k_i are the individual mass transfer coefficients. $\hat{V}_{ig}$ is the partial specific volume of component *i* in the gas phase, *z(t)* is the solution-air interface, and h^G is the air heat coefficient. T^G, $\Delta\hat{H}_{vi}$, $\hat{C}_p^p$, $\hat{C}_p^s$, H represent the air temperature, heat of vaporization of solvent/nonsolvent, specific heat capacity of the polymer solution, specific heat capacity of substrate, and thickness of substrate, respectively.

The energy equation in Equation (3.1.8) is dimensionalized using the dimensionless time in Equation (3.1.5) together with the following coordinate transformations to facilitate numerical computation:

$$l^* = \frac{z(t)}{L} \tag{3.1.9}$$

$$T^* = \frac{T - T_0}{T^G - T_0} \tag{3.1.10}$$

where T_0 is the initial temperature of the solution.

The final dimensionless energy equation becomes [28]:

$$\frac{dT^*}{dt^*} = \frac{A(1 - T^*) + B + C}{D + l^*} \tag{3.1.11}$$

$$A = \frac{Lh^G}{D_0 \rho^P \hat{C}_p^P} \tag{3.1.12}$$

$$B = -\frac{Lk_1(y_{1gt} - y_{1gx})\Delta\hat{H}_{v1}}{\hat{V}_{1g}\rho^P \hat{C}_p^P D_0 (T^G - T_0)} \tag{3.1.13}$$

$$C = -\frac{Lk_2(y_{2gl} - y_{2g\infty})\Delta\hat{H}_{v2}}{\hat{V}_{2g}\rho^P\hat{C}_P^P D_0(T^G - T_0)} \tag{3.1.14}$$

$$D = \frac{\rho^s\hat{C}_p^s H}{\rho^p\hat{C}_p^p L} \tag{3.1.15}$$

Assuming the casting film is initially uniform, the following initial conditions apply:

$$\phi_1(0,\eta) = \phi_{10}(\eta) \quad for\ 0 \le \eta \le 1 \tag{3.1.16}$$

$$\phi_2(0,\eta) = \phi_{20}(\eta) \quad for\ 0 \le \eta \le 1 \tag{3.1.17}$$

$$l(0) = L \tag{3.1.18}$$

$$T(0) = T_0 \tag{3.1.19}$$

The mass transfer boundary conditions at the interface can be written as follows:

$$\frac{d}{dt}\left(l\int_0^1 \phi_1 d\eta\right) = -k_1\hat{V}_1\left(y_{1gl} - y_{1g\infty}\right) \qquad at\ \eta = 1 \tag{3.1.20}$$

$$\frac{d}{dt}\left(l\int_0^1 \phi_2 d\eta\right) = -k_2\hat{V}_2\left(y_{2gl} - y_{2g\infty}\right) \qquad at\ \eta = 1 \tag{3.1.21}$$

The thickness of the film is determined by the material balance for the polymer as:

$$l = L\frac{\int_0^1 \phi_{30} d\eta}{\int_0^1 \phi_3 d\eta} \tag{3.1.22}$$

Since ideal gas and equilibrium are assumed, the solvent/nonsolvent composition at the gas side of the interface can be written in terms of the solvent/nonsolvent activity on the polymer film side, a_i, as:

$$\rho_{igl} = \frac{a_i P_i^{sat}}{\hat{V}_{ig} P} \tag{3.1.23}$$

where P is the total pressure and P_i^{sat} is the vapor pressure of component i.

Activities for the ternary system are evaluated from Flory-Huggins theory [4], where the Gibbs free energy of mixing, ΔG_M, and chemical potential, μ_i, are given in Equations (2.1.1) and (2.1.2) respectively. Thus, the expressions for a_i are:

$$a_1 = \phi_1 \exp\left[(1-\phi_1)(1+g_{12}\phi_2+g_{13}\phi_3) - \frac{v_1}{v_2}\phi_2\left(1+g_{23}\phi_3+u_1u_2\frac{v_2}{v_1}\frac{dg_{12}}{du_2}+\phi_3^2\frac{dg_{23}}{d\phi_3}\right) - \frac{v_1}{v_3}\phi_3\right] \tag{3.1.24}$$

$$a_2 = \phi_2 \exp\left[(1-\phi_2)\left(1+g_{12}\frac{v_2}{v_1}\phi_1+g_{23}\phi_3\right) - \frac{v_2}{v_1}\phi_1\left(1+g_{13}\phi_3-u_1u_2\frac{dg_{12}}{du_2}\right) - \phi_3\left(\frac{v_2}{v_3}+\phi_2\phi_3\frac{dg_{23}}{d\phi_3}\right)\right] \tag{3.1.25}$$

where v_i is the molar volume of component i, g_{ij}'s are the concentration dependent binary interaction parameters, $u_1 = \phi_1/(\phi_1+\phi_2)$, and $u_2 = \phi_2/(\phi_1+\phi_2)$.

3.2 Diffusion model

The multicomponent diffusivities are evaluated with a friction-based diffusion model recently proposed by Alsoy and Duda [28]:

$$D_{11} = \frac{\phi_1}{\hat{V}_1}(1-\phi_1)D_1\left(\frac{\hat{V}_1}{RT}\frac{\partial\Delta\mu_1}{\partial\phi_1}\right) - \frac{\phi_1\phi_2 D_2}{\hat{V}_1}\left(\frac{\hat{V}_1}{RT}\frac{\partial\Delta\mu_2}{\partial\phi_1}\right) \tag{3.2.1}$$

$$D_{12} = \frac{\phi_1}{\hat{V}_1}(1-\phi_1)D_1\left(\frac{\hat{V}_2}{RT}\frac{\partial\Delta\mu_1}{\partial\phi_2}\right) - \frac{\phi_1\phi_2 D_2}{\hat{V}_1}\left(\frac{\hat{V}_2}{RT}\frac{\partial\Delta\mu_2}{\partial\phi_2}\right) \tag{3.2.2}$$

$$D_{21} = \frac{\phi_2}{\hat{V}_2}(1-\phi_2)D_2\left(\frac{\hat{V}_1}{RT}\frac{\partial\Delta\mu_2}{\partial\phi_1}\right) - \frac{\phi_1\phi_2 D_2}{\hat{V}_2}\left(\frac{\hat{V}_1}{RT}\frac{\partial\Delta\mu_1}{\partial\phi_1}\right) \tag{3.2.3}$$

$$D_{22} = \frac{\phi_2}{\hat{V}_2}(1-\phi_2)D_2\left(\frac{\hat{V}_2}{RT}\frac{\partial\Delta\mu_2}{\partial\phi_2}\right) - \frac{\phi_1\phi_2 D_1}{\hat{V}_2}\left(\frac{\hat{V}_2}{RT}\frac{\partial\Delta\mu_1}{\partial\phi_2}\right) \tag{3.2.4}$$

where $\frac{\partial \Delta\mu_i}{\partial \phi_i}$ is the derivative of chemical potential evaluated from Equations (2.1.3)-(2.1.6) and the D_i are the self diffusion coefficients predicted from Vrentas-Duda free volume theory as follows [29]:

$$D_1 = D_{01} \exp\left(\frac{-\left(\frac{\phi_1}{\hat{V}_1} \hat{V}_1^* + \frac{\phi_2}{\hat{V}_2} \hat{V}_2^* \zeta_{13} / \zeta_{23} + \frac{\phi_3}{\hat{V}_3} \hat{V}_3 \zeta_{13} \right)}{\hat{V}_{FH} / \gamma} \right) \tag{3.2.5}$$

$$D_2 = D_{02} \exp\left(\frac{-\left(\frac{\phi_1}{\hat{V}_1} \hat{V}_1^* \zeta_{23} / \zeta_{13} + \frac{\phi_2}{\hat{V}_2} \hat{V}_2^* + \frac{\phi_3}{\hat{V}_3} \hat{V}_3 \zeta_{23} \right)}{\hat{V}_{FH} / \gamma} \right) \tag{3.2.6}$$

$$\frac{\hat{V}_{FH}}{\gamma} = \frac{K_{11}}{\gamma}(K_{21} - T_{g1} + T)\frac{\phi_1}{\hat{V}_1} + \frac{K_{12}}{\gamma}(K_{22} - T_{g1} + T)\frac{\phi_2}{\hat{V}_2} + \frac{K_{13}}{\gamma}(K_{23} - T_{g3} + T)\frac{\phi_3}{\hat{V}_3} \tag{3.2.7}$$

where D_{0i} and $\hat{V}_i^*$ are the pre-exponential factor and specific critical hole free volume required for a jump of component *i*. K_{11} and K_{21} are free-volume parameters for nonsolvent, K_{12} and K_{22} are free-volume parameters for solvent, and K_{13} and K_{23} are those for polymer. ζ_{i3} is the ratio of molar volumes for nonsolvent/solvent and polymer jumping units. γ is the overlap factor and T_{gi} is the glass transition temperature of component *i*.

3.3 Determination of Model Parameters

Free volume and interaction parameters for the ternary cellulose acetate/acetone/water system are given by Altinkaya et. al. [9] and those for the binary

poly(vinylidene fluoride)/dimethyl formamide are reported by Matsuyama et. al. [11]. Values are listed in Table 3.3.1. The free volume parameters for the PSF/NMP and PEI/NMP systems are estimated using the Vrentas-Duda free volume theory.

$\hat{V}_i^*$ is estimated as the specific volume of component *i* at 0 K which can be obtained using group contribution methods [30]. The ratio of ζ_i's can be written as [30]:

$$\frac{\zeta_{13}}{\zeta_{23}} = \frac{M_1 \hat{V}_1^*}{M_2 \hat{V}_2^*} \tag{3.3.1}$$

where ζ_{23} is defined as [30]:

$$\zeta_{23} = \frac{M_2 \hat{V}_2^*}{V_{3j}} \tag{3.3.2}$$

in which V_{3_j} is the molar volume of the polymer jumping unit and it is estimated from the polymer glass transition temperature using the following correlation [30]:

$$V_{3j}\left(\frac{cm^3}{mol}\right) = 0.6224 T_{g3}(^oK) - 86.95 \tag{3.3.3}$$

The glass transition temperatures used for polysulfone and polyetherimide are 459K and 480.5K respectively. The polymer free volume parameters ($\frac{K_{13}}{\gamma}$ and K_{23}) for polysulfone and polyetherimide are estimated from viscosity data. The temperature dependencies of the viscosity of pure polymer are usually expressed in terms of the Williams-Landel-Ferry equation [31]:

$$\log\left(\frac{\eta_3(T)}{\eta_3(T_{g3})}\right) = \frac{-C_{13}^{WLF}(T - T_{g3})}{C_{23}^{WLF} - T_{g3} + T} \tag{3.3.4}$$

The free volume parameters for the polymer are related to the WLF constants as follows [31]:

$$K_{23} = C_{23}^{WLF} \tag{3.3.5}$$

$$\frac{K_{13}}{\gamma} = \frac{\hat{V}_3^*}{2.303 C_{13}^{WLF} C_{23}^{WLF}} \tag{3.3.6}$$

The values of C_{13}^{WLF} and C_{23}^{WLF} for polysulfone are 15.1 and 49 respectively [32], and the values of C_{13}^{WLF} and C_{23}^{WLF} for polyetherimide are 17.0 and 37.5 respectively [33].

The solvent-nonsolvent interaction parameter, g_{12} for the CA/acetone/water system is assumed to be constant since: (1) Yilmaz et al. [24] have shown that shapes of the binodal and spinodal curves generated from constant and concentration dependent solvent-nonsolvent interaction parameters for the same system are similar, and (2) Concentration dependent solvent-nonsolvent interaction parameter causes numerical instability related to the prediction of negative main diffusivities (D_{11} & D_{22}). The free volume parameters and the Flory-Huggins interaction parameters for PSF/NMP/water and PEI/ NMP/water systems, together with their references are listed in Table 3.3.1. Other model parameters such as the physical properties are listed in Tables 3.3.2 and 3.3.3.

Parameter	CA/acetone/water	PVDF/DMF/water	PSF/NMP/water	Ref.	PEI/NMP/water	Ref.
$\hat{V}_2^*$ (cm^3/g)	0.943	0.926	0.841	30	0.841	30
$\hat{V}_3^*$ (cm^3/g)	2.67	0.565	0.733	30	0.663	30
D_{02} (cm^2/s)	3.6×10^{-4}	8.48×10^{-4}	3.137×10^{-4}	34	3.137×10^{-4}	34
ζ_{13}	0.0943	0.313	0.097	30	0.0909	30
ζ_{23}	0.268	1.1	0.4194	30	0.393	30
K_{12}/γ ($cm^3/g\,K$)	0.00186	0.000976	0.000963	34	0.000963	34
K_{13}/γ ($cm^3/g\,K$)	0.000364	0.000273	0.00043	31	0.000452	31
$K_{22}-T_{g2}$ (K)	-53.33	-43.8	-48.496	34	-48.496	34
$K_{23}-T_{g3}$ (K)	-240	-127	-410	31	-443	31
g_{12}	1.3	$0.5+0.04u_2+0.8u_2^2-1.2u_2^3+0.8u_2^4$	$0.785+0.665u_2$	35	$0.785+0.665u_2$	35
g_{23}	0.5	0.43	0.24	35	0.507	36
g_{13}	1.4	2.09	3.7	35	2.1	37

Table 3.3.1: Free volume and Flory-Huggins interaction parameters used in different systems.

Parameter	Value	Parameter	Value
$\hat{V}_1^*$ (cm^3/g)	1.071	D_0 (cm^2/s)	1.0×10^{-5}
D_{01} (cm^2/s)	8.55×10^{-4}	ρ^s (g/cm^3)	2.5
K_{11}/γ (cm^3/g K)	0.00218	$\hat{C}_p^s$ (J/g K)	0.75
$K_{21}-T_{g1}$ (K)	-152.29	k^G (W/cm K)	2.55×10^{-4}
M_1 (g/mol)	18.0	μ_g (Pa s)	1.85×10^{-5}
ρ_1 (g/cm^3)	1.0	D_{1g} (cm^2/s)	0.267
v_1 (cm^3/mol)	18.0	$y_{2g\infty}$	0.0
$\Delta\hat{H}_{v1}$ (J/g)	2444	H (cm)	0.5

Table 3.3.2: Model parameters common to the four polymer systems.

Parameter	CA/Acetone	PVDF/DMF	PSF/NMP	PEI/NMP
M_2 (g/mol)	58.08	73.1	99.1	99.1
M_3 (g/mol)	307000	534000	20270	22400
ρ_2 (g/cm^3)	0.79	0.9443	1.03	1.03
ρ_3 (g/cm^3)	1.31	1.739	1.24	1.27
v_2 (cm^3/mol)	73.92	77.4	96.22	96.22
v_3 (cm^3/mol)	30532	307000	16347	17638
D_{2g} (cm^2/s)	0.128	0.023	0.0075	0.0075
$\Delta\hat{H}_{v2}$ (J/g)	552	651	533	533
L_c (cm)	10	1	5	10

Table 3.3.3: Model parameters unique to the four polymer systems.

3.4 Heat and Mass Transfer Coefficients

Mass transfer coefficients for free and forced convection can be determined by the empirical correlations [38, 39] given below:

$$\frac{k_i L_c y_{air,lm}}{D_{ig}} = 0.27(Gr * Sc_i)^{0.25} \qquad \text{Free convection} \qquad (3.4.1)$$

$$\frac{k_i L_c y_{air,lm}}{D_{ig}} = 0.27\,\mathrm{Re}^{0.5}\, Sc_i^{\,0.33} \qquad \text{Forced convection} \qquad (3.4.2)$$

where $y_{air,lm}$ is the log mean mole fraction difference of air and L_c is the characteristic length of the film surface. D_{ig} is the mutual diffusion coefficient of component *i* in the air-solvent/nonsolvent gas phase. The Schmidt and Reynolds numbers have their standard definitions:

$$Sc_i = \frac{\mu_g}{\rho_g D_{ig}} \qquad (3.4.3)$$

$$\mathrm{Re} = \frac{\rho_g u_\infty L_c}{\mu_g} \qquad (3.4.4)$$

where ρ_g, μ_g, and u_∞ represent the total mass density of gas phase, viscosity of gas mixture, and air velocity, respectively.

The corrected Grashof number which incorporates both the concentration and temperature effects on the variation in gas-phase density is given by the following:

$$Gr = \frac{L_c^{\,3}\rho_g^{\,2} g}{\mu_g^{\,2}}\left|\xi_h (T - T^G) + \xi_{m1}(y_{1gl} - y_{1g\infty}) + \xi_{m2}(y_{2gl} - y_{2g\infty})\right| \qquad (3.4.5)$$

where g is the gravitational constant and T^G is the air temperature. The coefficient ξ_h represents the temperature effect on the gas density and is given by:

$$\xi_h = -\frac{1}{\rho_g}\left(\frac{\partial \rho_g}{\partial T}\right)_{P,y_i} \qquad (3.4.6)$$

where P is the pressure, T is the temperature and ρ_g is evaluated from ideal gas law. The coefficients ξ_{mi} represent the effect of the concentration profile on the gas density and are given by:

$$\xi_{mi} = -\frac{1}{\rho_g}\left(\frac{\partial \rho_g}{\partial y_i}\right)_{P,T} \tag{3.4.7}$$

The free-convection and forced-convection heat transfer coefficients for solvent/nonsolvent are given by the following expressions [38, 39].

$$\frac{hL_c}{k^G} = 0.27(Gr * \Pr)^{0.25} \qquad \text{Free convection} \tag{3.4.8}$$

$$\frac{hL_c}{k^G} = 0.664\,\mathrm{Re}^{0.5}\,\Pr^{0.33} \qquad \text{Forced convection} \tag{3.4.9}$$

where k^G is the air thermal conductivity and Pr is the Prandtl number.

3.5 Other Parameters

The saturated vapor pressures of solvent/nonsolvent are calculated from two different equations depending on the available data. Saturated vapor pressures of acetone and water are calculated from Equation (3.5.1) [9] while that of DMF and NMP are calculated from Equation (3.5.2) [40, 41]. The constants used in equations (3.5.1) and (3.5.2) are given in Table 3.5.1. The critical temperatures of water and acetone are 647.3 K and 508.1 K respectively, and the critical pressures of water and acetone are 221.2 kPa and 47 kPa respectively.

$$\ln\frac{P^{sat}}{P_c} = \frac{A(1-T_r) + B(1-T_r)^{1.5} + C(1-T_r)^3 + D(1-T_r)^6}{T_r} \tag{3.5.1}$$

$$\log P^{sat} = A - \frac{B}{T + C} \tag{3.5.2}$$

where P is in kPa and T is in K in both equations.

Parameter	Water	Acetone	DMF	NMP
A	-7.76451	-7.45514	6.03823	6.3213
B	1.45838	1.202	1393.225	1709.28
C	-2.7758	-2.43926	-77.428	-79.04
D	-1.23303	-3.3559	-	-

Table 3.5.1: The constants used in the calculation of vapor pressure of water, acetone, DMF and NMP.

3.6. Numerical Algorithm

The ternary phase diagrams for the systems modeled here were generated using the algorithm developed by Yilmaz and McHugh [24]. The coupled, nonlinear partial differential equations were solved numerically using finite difference approximation with a variable grid size and the details of the finite difference equations were given by Tsay and McHugh [42]. The variable grid size is set up to generate a finer mesh near the interface since concentration gradients are steeper there. The distance, h_i, between two successive nodes for a space domain between x = 0 and x = L is given as follows [43]:

$$h_i = h_{i-1}\left(1+\frac{\alpha}{\pi}\left(1-\frac{x_i}{L}\right)^{\beta} h_{i-1}\right) \tag{3.6.1}$$

where α and β are constant parameters for adjusting the grid size. With $\alpha > 0$ the form tends cut down the increase of h_i as i increases. The network with $\beta > 0$ has larger grid intervals near x = L and smaller in the vicinity of x = 0. For $\beta < 0$, grid density is larger near x = L and smaller near x = 0. α and β were chosen to be 7.0 and 1.0 respectively to obtain optimum grid network. The boundary conditions were solved using an IMSL routine called DNEQNF. In order to reduce the stiffness of the partial differential equations for systems having low or essentially zero nonsolvent concentration, a variable

time step was applied where it is adjusted based on the differences in the predicted and corrected solutions [44]. The deviation E, is defined as follows:

$$E = \max\left|x_{init} - x\right| \tag{3.6.2}$$

where x_{init} is the initial guess.

The absolute deviation E is compared to a target value E_t which is set to be 1×10^{-8} in this model. If E is within 5% of E_t, the current time step is not changed. If E is below the target value, time step is increased for the next time step using the following expression [44]:

$$\Delta t = \left(\frac{E_t}{2E}\right)^{1/6} \Delta t \tag{3.6.3}$$

For numerical stability, the increase is limited by a maximum of 50% and a minimum of 20%. If the absolute error E is larger than the target value, time step is decreased using Equation (3.6.3) and the new solution vector is obtained with smaller time step. The accuracy of the numerical algorithm is confirmed by increasing the number of grid points and it is shown in Figure 3.6.1.

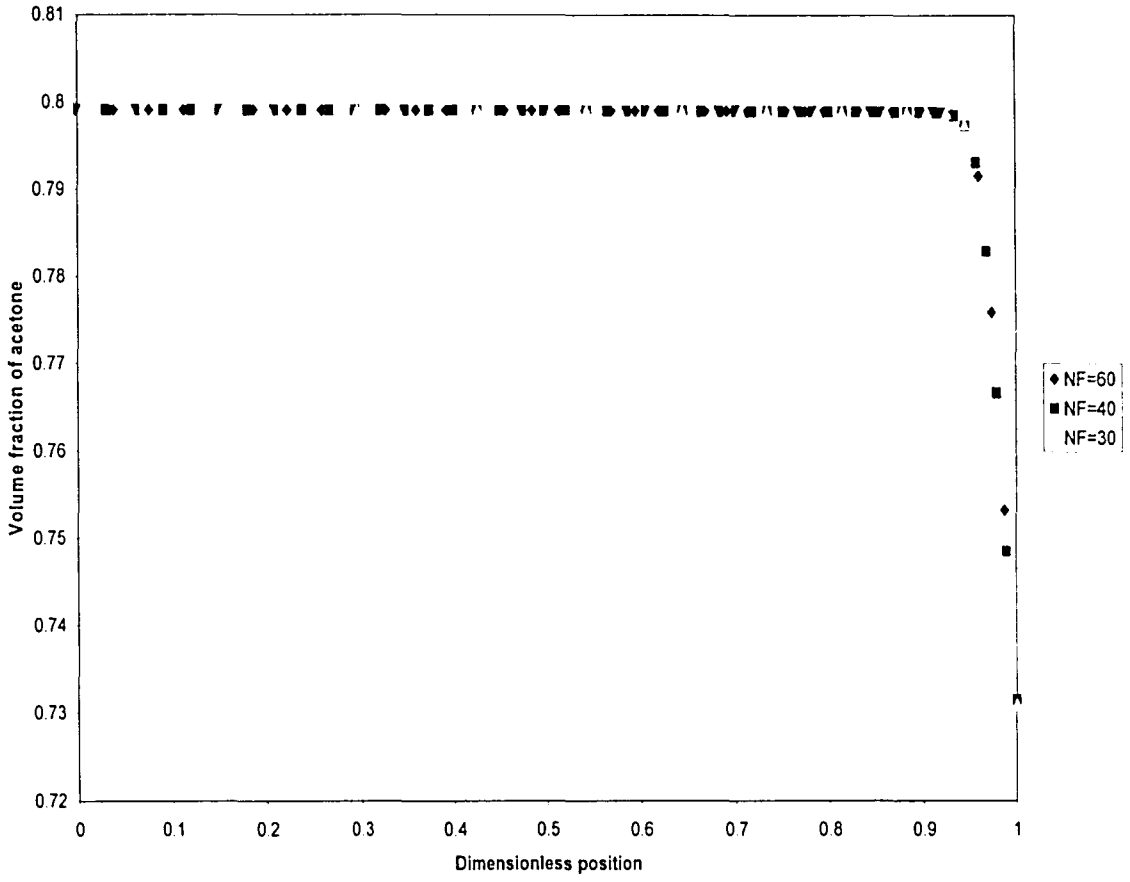

Figure 3.6.1: Acetone concentration profile in the casting film for different number of grid points used.

Chapter 4

Results for Dry-Casting

Results are shown for the simulations of the cellulose acetate/acetone/water system that illustrate the effect of different operating conditions like initial nonsolvent concentration and film thickness, evaporation temperature, air velocity and relative humidity in the dry-casting process. The role of diffusion formalism is also illustrated to show the accuracy of the multicomponent diffusion theory. The input parameters used for the different simulations for dry-casting is shown in Table 4.1.1.

4.1 Effect of initial nonsolvent concentration

In order to understand the phase inversion kinetics in dry-casting, mass transfer paths that describe solution-air interface composition and variation with time is calculated from the model. By superposing mass transfer paths onto the ternary phase diagram, a number of detailed morphological features can be predicted. Predictions of composition and temperature profiles, mass and heat transfer coefficients, water and acetone flux at the solution-air interface, and thickness of the film are shown in Figures 4.1.1-4.1.8 for conditions listed as Case A2 in Table 4.1.1. Because of its high vapor pressure, the drying rate of acetone is much faster than that of water, particularly during the initial stage of dry-casting. As seen in Figures 4.1.1-4.1.3, this also leads to a very

sharp concentration gradient of acetone at the interface, especially for short times. As shown in Figure 4.1.4, the difference between the fluxes of water and acetone at the interface is largest for times less than 15s when only acetone is evaporating from the film. It also indicates that both the interfacial fluxes, and hence the drying rates of water and acetone, decrease throughout the process, and finally become equal shortly after the onset of phase separation at 250s. It is interesting to note that the flux of water is negative during the first 15s period. Because the large concentration gradient of acetone at the interface makes the cross diffusion coefficient, D_{12} positive in Equation (3.1.3) and water behaves as if it is diffusing into the film instead of evaporating from the film. The air heat transfer coefficient and mass transfer coefficient of water and acetone shown in Figures 4.1.5 and 4.1.6 decrease linearly with time due to the decrease in drying rates. The mass transfer coefficient of water is larger than that of acetone because the mutual diffusion coefficient of water in the air-water gas phase is higher.

Case	System	ϕ_i			T_0 (K)	T_g (K)	L (cm)	Relative humidity (%)	Mode of convection
		$i=1$	$i=2$	$i=3$					
A1	CA / acetone / water	0.15	0.75	0.1	296	297	0.02	0	Free
A2	CA / acetone / water	0.1	0.8	0.1	296	297	0.02	0	Free
A3	CA / acetone / water	0.08	0.82	0.1	296	297	0.02	0	Free
A4	CA / acetone / water	0.05	0.85	0.1	296	297	0.02	0	Free
A5	CA / acetone / water	0.02	0.88	0.1	296	297	0.02	0	Free
A6	CA / acetone / water	0.1	0.8	0.1	296	297	0.03	0	Free
A7	CA / acetone / water	0.1	0.8	0.1	296	323	0.02	0	Free
A8	CA / acetone / water	0.08	0.82	0.1	296	297	0.02	0	Forced, $u_\infty = 10$cm/s
A9	CA / acetone / water	0.08	0.82	0.1	296	297	0.02	0	Forced, $u_\infty = 50$cm/s
A10	CA / acetone / water	0.08	0.82	0.1	296	297	0.02	0	Forced, $u_\infty = 200$cm/s
A11	CA / acetone / water	0.1	0.8	0.1	296	297	0.02	50	Free

Table 4.1.1: Input parameters used for simulations in dry-casting.

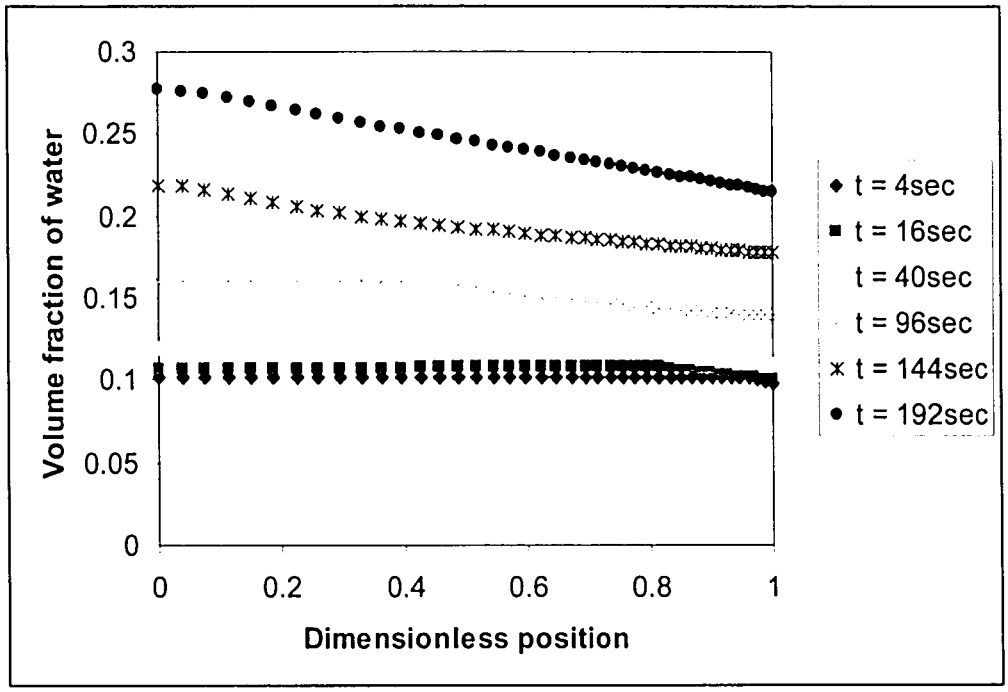

Figure 4.1.1: Concentration profiles of water in the cellulose/acetone/water system at different times for the conditions listed as A2 in Table 4.1.1.

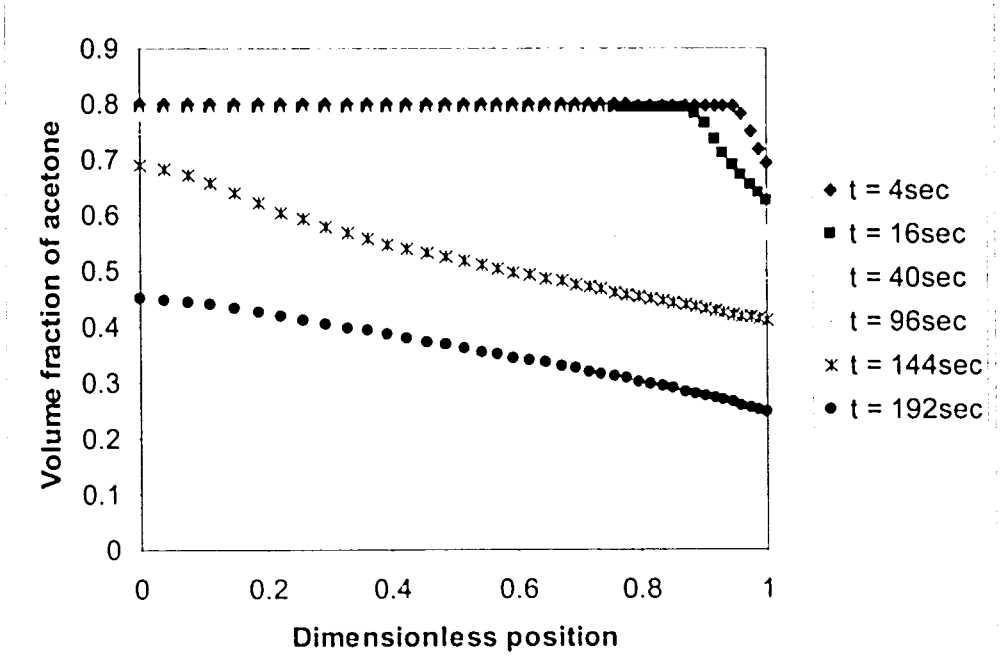

Figure 4.1.2: Concentration profile of acetone in the cellulose acetate/acetone/water system at different times for the conditions listed as A2 in Table 4.1.1.

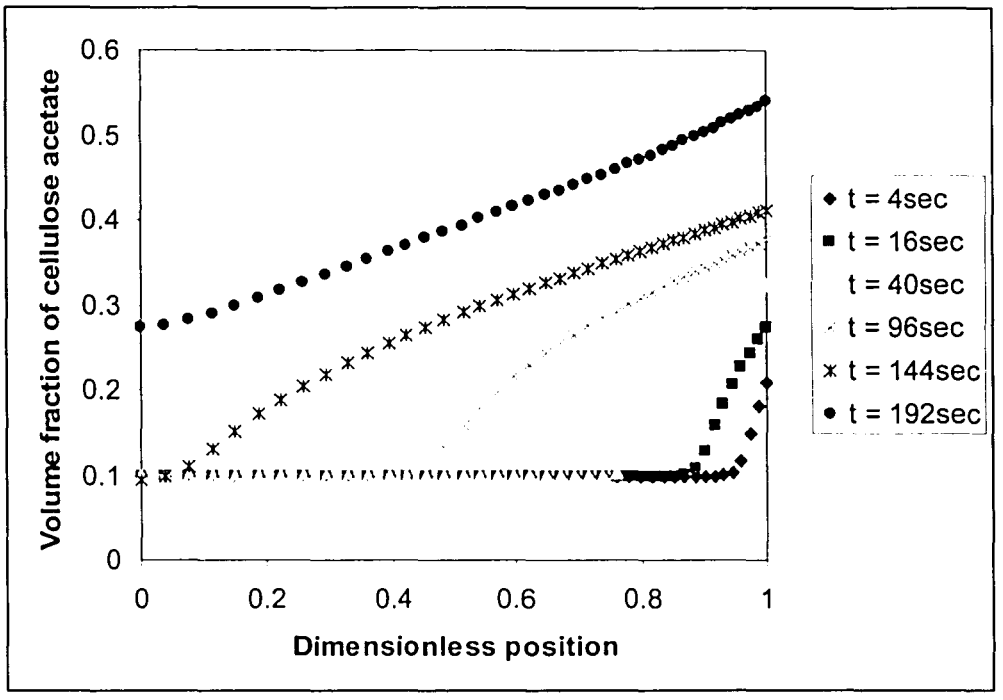

Figure 4.1.3: Concentration profile of cellulose acetate in the cellulose/acetone/water system at different times for the conditions listed as A2 in Table 4.1.1.

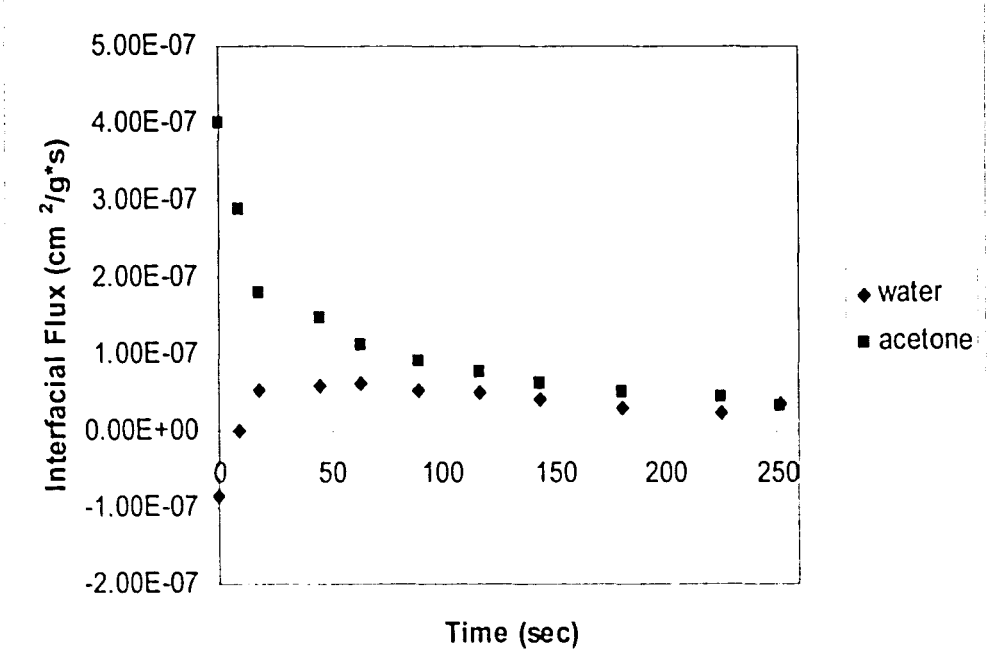

Figure 4.1.4: Fluxes of water and acetone at the interface for Case A2.

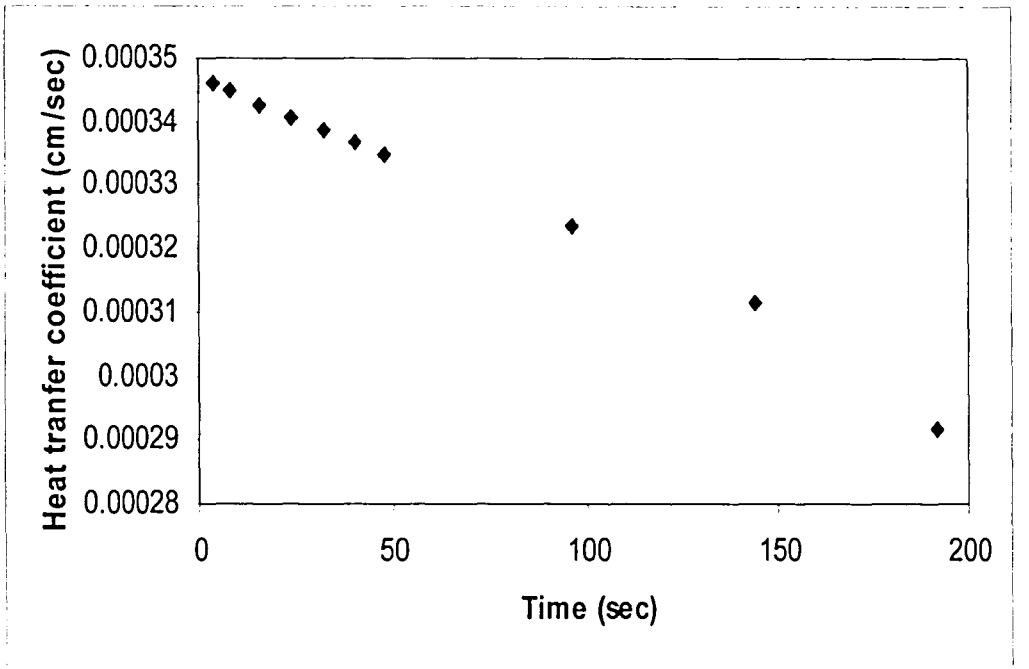

Figure 4.1.5: Change of heat transfer coefficient as a function of time for Case A2.

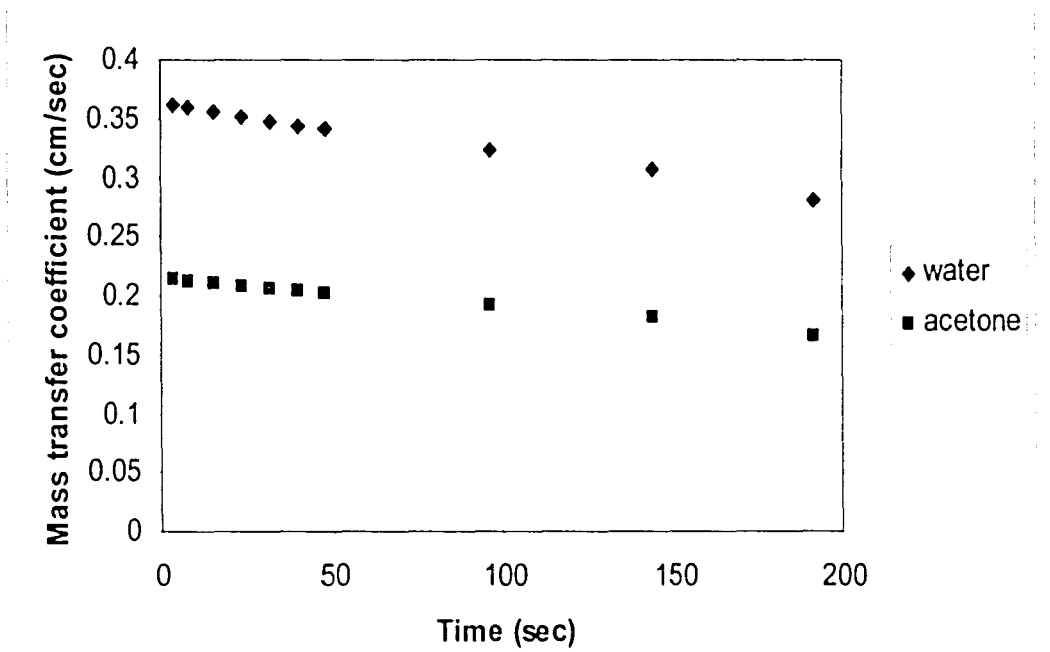

Figure 4.1.6: Change of mass transfer coefficients of water and acetone as a function of time for Case A2.

Since both water and acetone evaporate from the system, the total volume of the casting solution decreases and hence the initial casting solution undergoes shrinkage. As we can see from Figure 4.1.7, there is an almost 75% decrease in the overall thickness of the film for Case A2. Due to the significant acetone and water loss from the film, there is also a significant cooling effect during the dry-casting process. An important aspect of the model is incorporating the effect of evaporative cooling by solving the energy equation with the assumption of uniform temperature throughout the polymer film. The temperature profile for Case A2 shown in Figure 4.1.8 indicates that the temperature decreases from 296 K to 288 K during the evaporation. This cooling effect is due to the temperature dependence of mass and heat transfer coefficients, ternary diffusivities and vapor pressures of acetone and water used in the model.

Simulations were carried out to investigate the effect of nonsolvent in the casting solution by holding the volume fraction of cellulose acetate constant at 0.1 while varying the volume fraction of water from 0.02 to 0.15. The simulations are denoted by Cases A1, A2, A3, A4 and A5 respectively. The mass transfer paths shown in Figure 4.1.9 indicate that phase separation occurs at the interface for initial water volume fractions greater than about 0.08. This is the minimum amount of water required in the initial casting solution containing 0.1 volume fraction of cellulose acetate for evaporation under dry atmosphere at an initial temperature of 296 K, air temperature of 297 K and initial film thickness of 0.02 cm. The results show the expected trend of increasing precipitation time with decreasing water concentration in the initial casting solution. Concentration profile of cellulose acetate at the moment of precipitation for Cases A1, A2 and A3 in Figure 4.1.10 show steeper concentration gradients at the interface and more shrinkage for casting

solutions having lower initial water concentration. This suggests the formation of dense structure and thick skin. Altinkaya's experimental results [10] also show that the membrane becomes more dense and the thickness of the dense top layer increases with lower initial water concentration in casting solution.

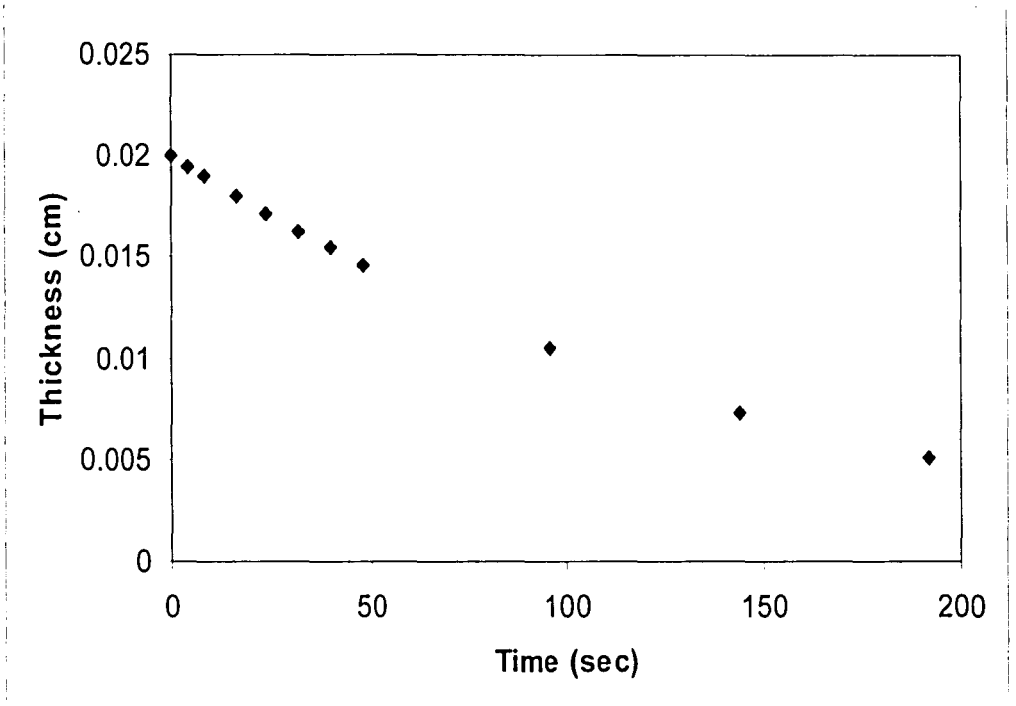

Figure 4.1.7: Change of polymer solution thickness as a function of time for Case A2.

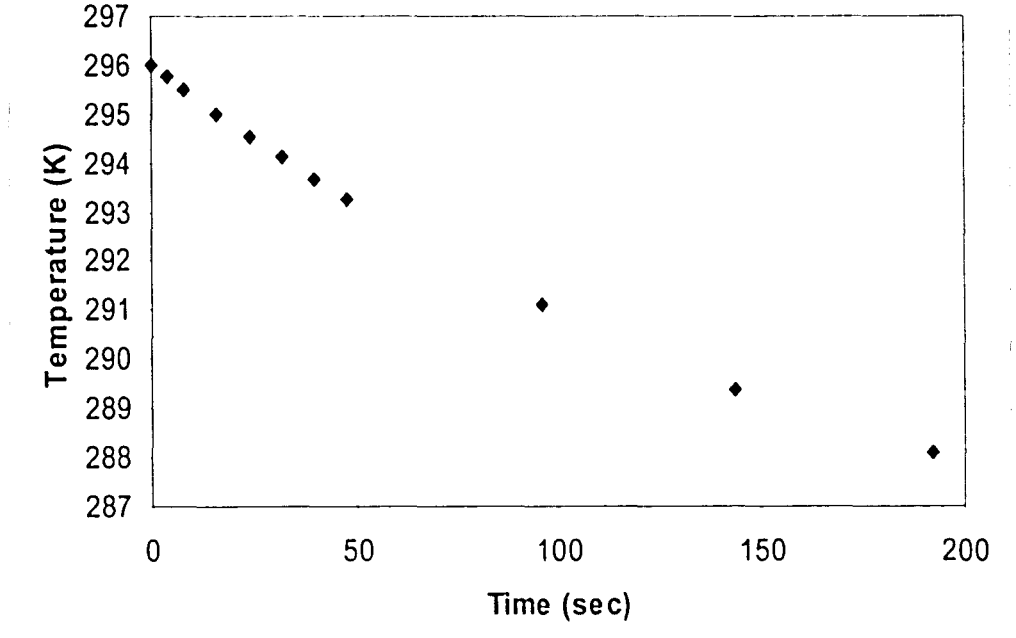

Figure 4.1.8: Change of polymer solution temperature as a function of time for Case A2.

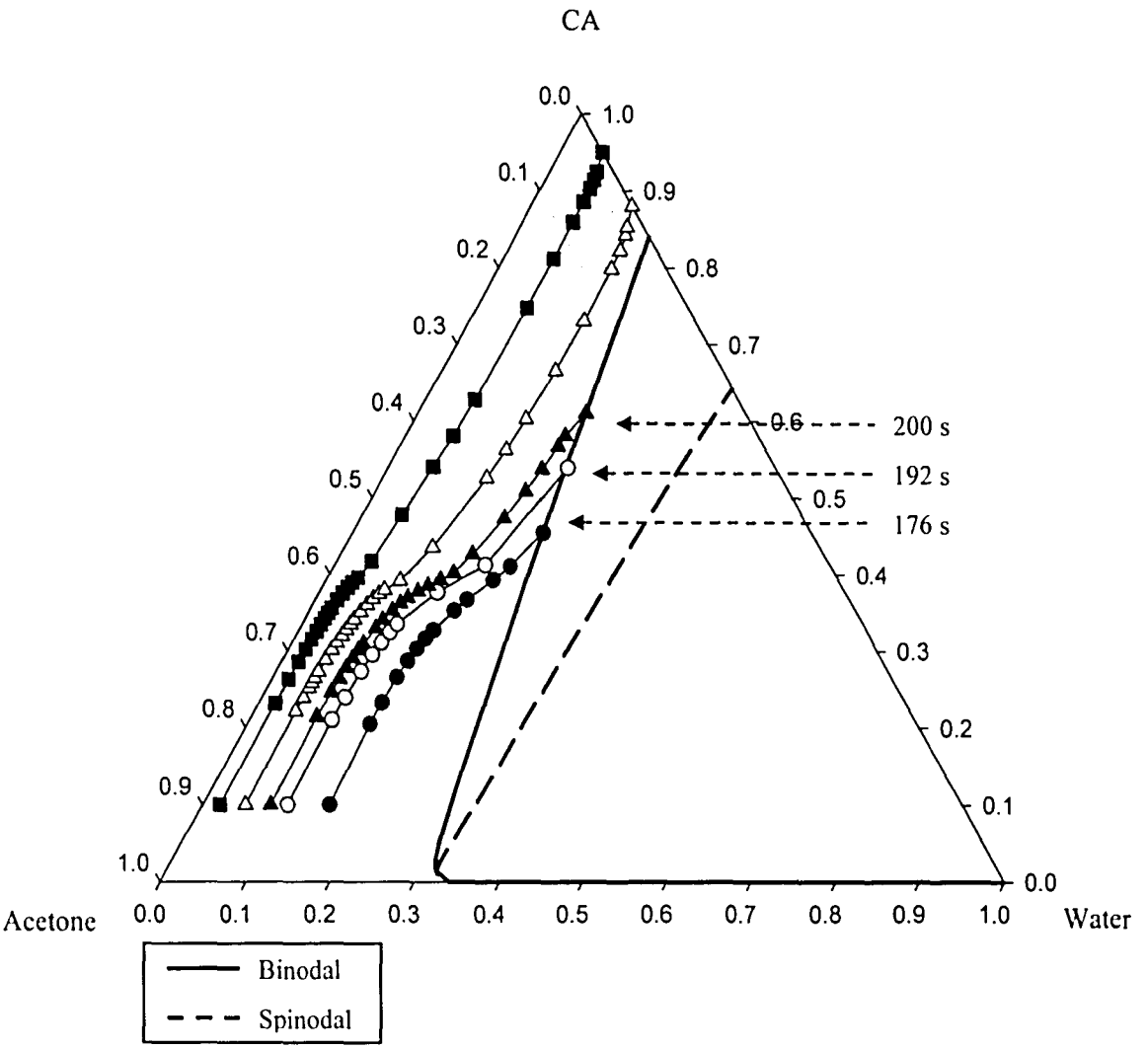

Figure 4.1.9: Mass transfer paths of cellulose acetate, acetone and water at the solution/air interface for various times for various initial water concentrations listed as cases A1 (●), A2 (○), A3 (▲), A4 (△) and A5 (■) in Table 4.1.1.

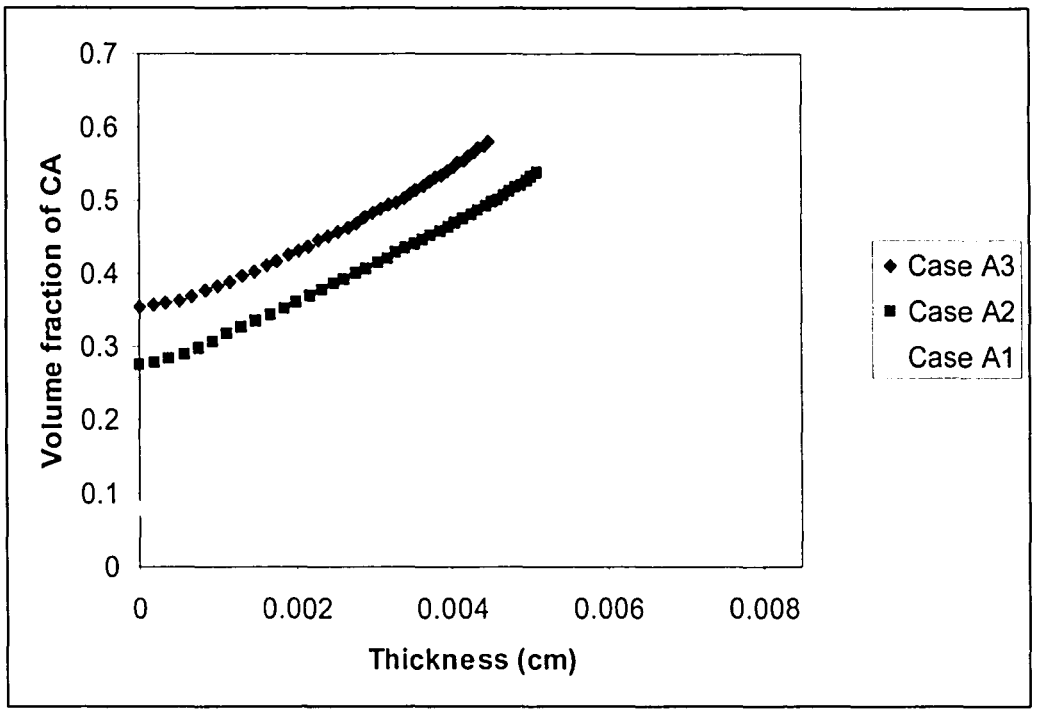

Figure 4.1.10: Concentration profile of cellulose acetate at the moment of precipitation for Cases A1, A2 and A3.

4.2 Effect of initial film thickness of the casting solution

To investigate the effect of initial film thickness in the casting solution, two different initial film thicknesses of 0.02 cm and 0.03 cm are compared. The simulations are denoted by Cases A2 and A6 respectively. All the other input parameters for Case A6 are identical to those of Case A2. As can be seen, decreasing initial film thickness leads to decreasing precipitation time, hence faster phase separation. The mass transfer paths for Cases A2 and A6 in Figure 4.2.1 show that the precipitation time for Case A2 is 192s while the precipitation time for Case A6 is 315s. Polymer concentration profiles for initial film thicknesses of 0.02cm and 0.03cm in Figure 4.2.2 indicate that the difference in polymer concentrations at the top and bottom surfaces becomes smaller with

decreasing initial film thickness. Similar prediction was reported by Matsuyama et al. [8] and Altinkaya et al. [10].

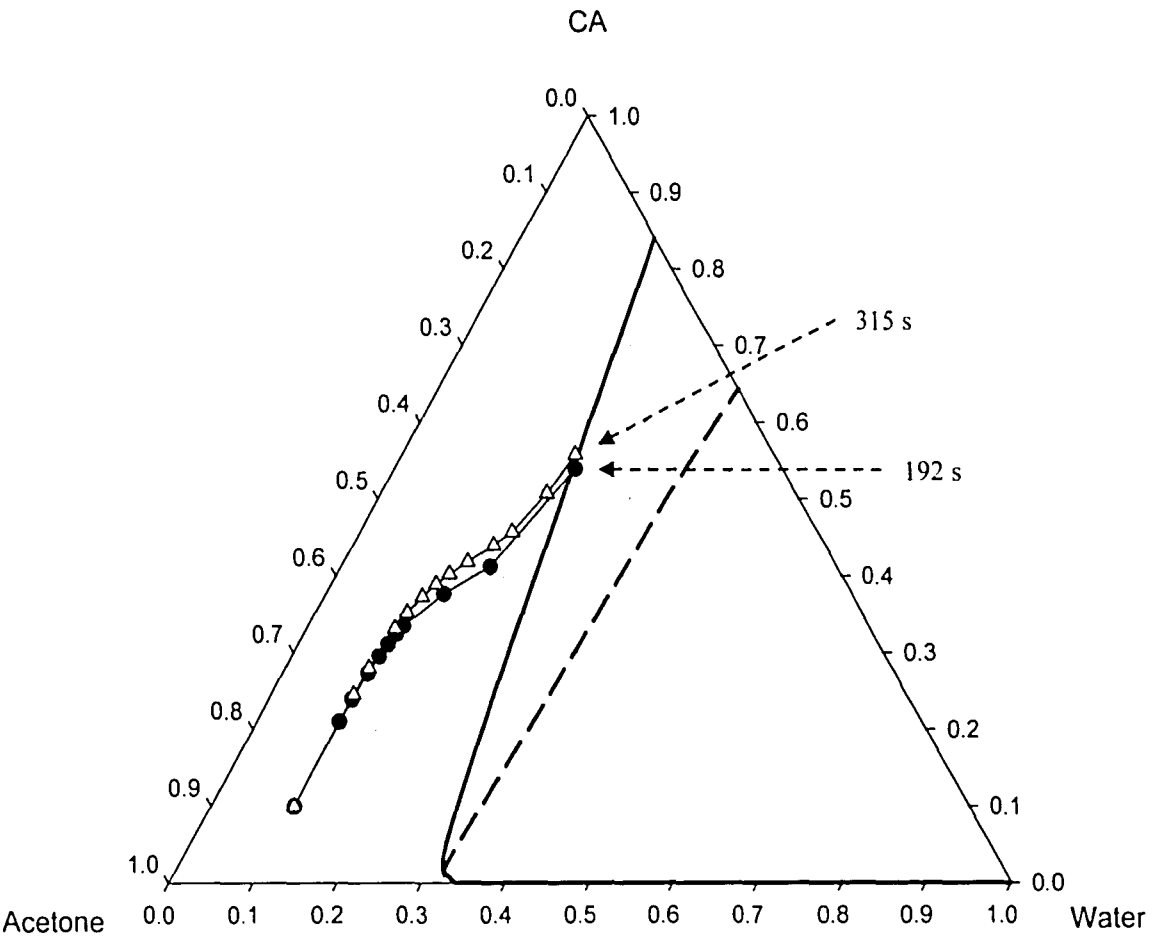

Figure 4.2.1: Mass transfer path of cellulose acetate, acetone and water at solution/air interface for two different film thicknesses listed as Cases A2 (●) and A6 (△) in Table 4.1.1.

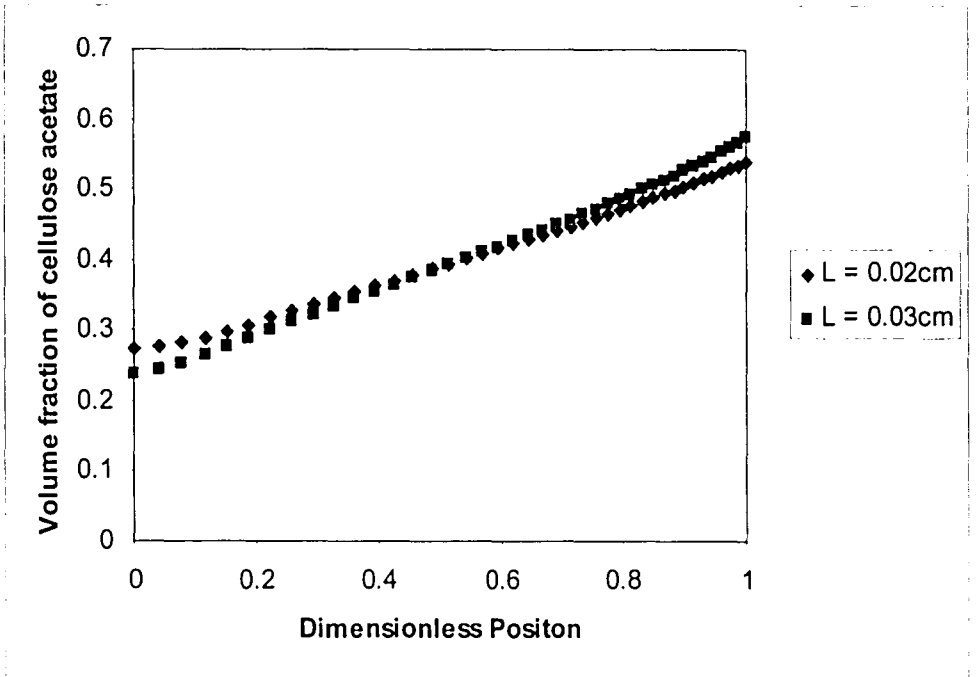

Figure 4.2.2: Polymer concentration profile for Cases A2 and A6 at the moment of precipitation.

4.3 Effect of evaporation temperature

The effect of evaporation temperature is investigated by comparing two different air temperatures at 297K and 323K. The simulations are denoted by Cases A2 and A7 respectively. All the other input parameters for Case A7 are identical to those of Case A2. As expected, increasing the air temperature leads to increased mass transfer rates for both the acetone and water in the film as well as faster evaporation from the solution-air interface. The results also show the expected trend of decreasing precipitation time with increasing air temperature in Figure 4.3.1. The mass transfer paths for the two cases are similar but the precipitation time for Case A2 is 192s while the precipitation time for Case A7 is 164s.

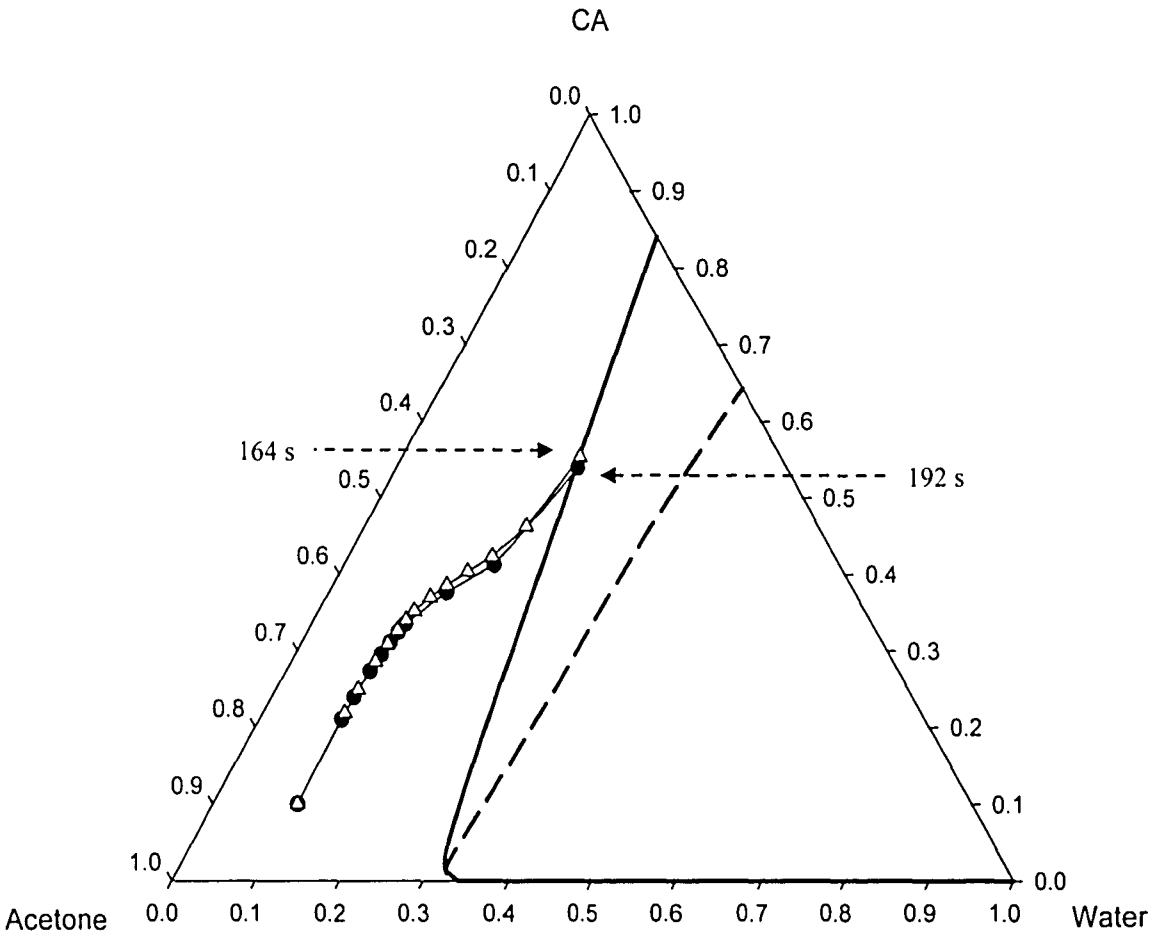

Figure 4.3.1: Mass transfer path of cellulose acetate, acetone and water at solution/air interface for two different evaporation temperatures listed as Cases A2 (●) and A7 (△) in Table 4.1.1.

4.4 Effect of evaporation conditions

In dry-casting, the evaporation of solvent and nonsolvent to the gas phase can be controlled either by free convection or forced convection processes. To investigate the effect of evaporation conditions, three simulations with different air velocities were performed. They are denoted by Cases A8, A9 and A10 in which the air velocities are 10cm/s, 50cm/s and 200cm/s respectively while all the other input parameters are kept the same as those in Case A3. Comparison of the mass transfer paths for these three cases is shown in Figure 4.4.1. While it is seen that increasing the air velocity not favor phase separation; however, it does increase the evaporation rate. The precipitation time for Case A8 is 152s while the precipitation time for Case A9 is 80s. As indicated before, phase separation is possible for Case A3 in which the evaporation is carried out under free convection. However, phase separation is completely suppressed and a uniformly dense structure will form when the evaporation is carried under forced convection and the air velocity is greater than 200cm/s. This agrees reasonably well with Altinkaya's experimental results [10] which show dense and non-porous structure for the film made under the same conditions.

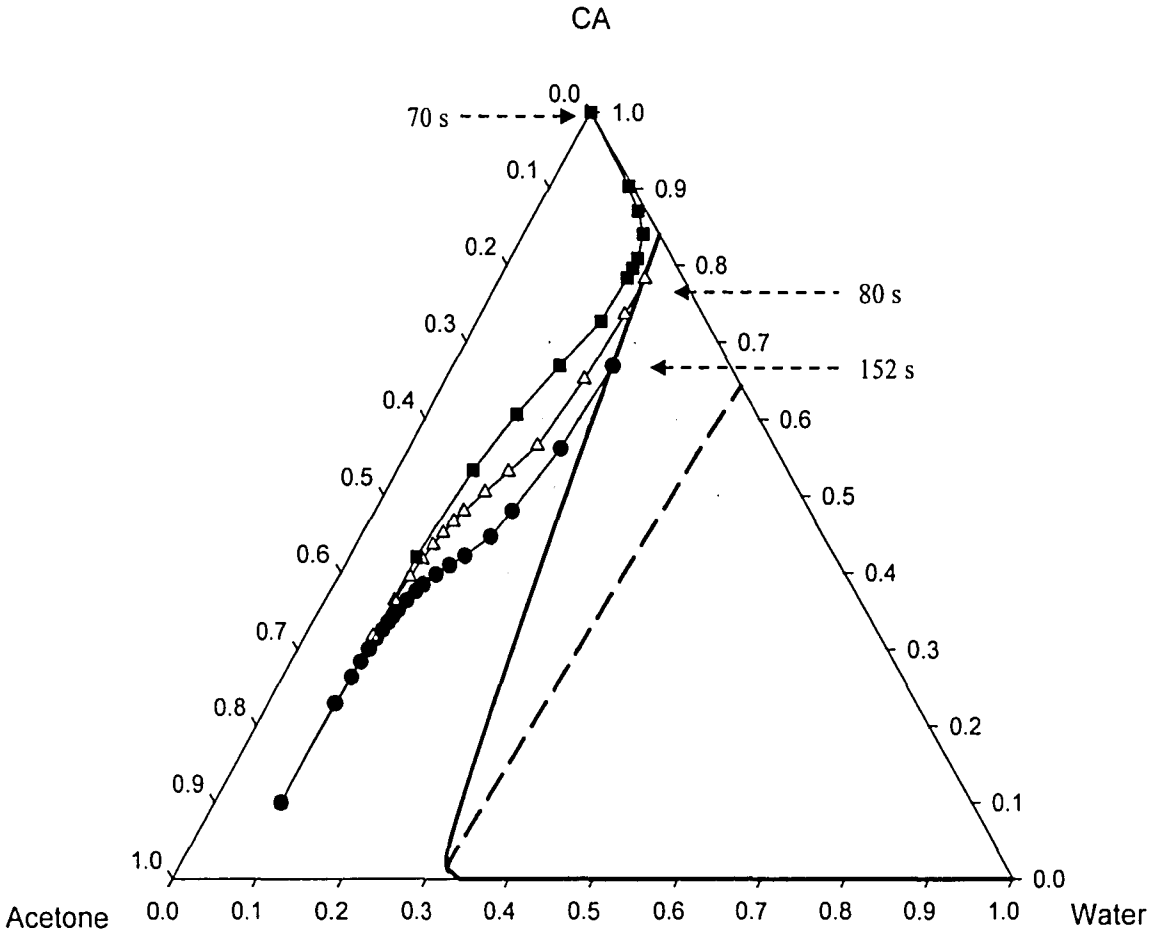

Figure 4.4.1: Mass transfer path of cellulose acetate, acetone and water at solution/air interface for free and forced convection corresponding to cases A8 (●), A9 (△) and A10 (■) in Table 4.1.1.

4.5 Effect of relative humidity

The relative humidity of the air plays an important role in the drying dynamics of the polymer film. In the process of dry-casting where the initial casting solution contains solvent, nonsolvent and polymer, increasing the relative humidity decreases the driving force for the evaporation of nonsolvent (usually water) thereby causing the solution-air interface to enter the binodal region more rapidly. To investigate the effect of relative humidity in dry-casting, two different relative humidities of 0% and 50%, respectively, are compared. The simulations are denoted by Cases A2 and A11 respectively. All the other input parameters for Case A11 are identical to those of Case A2. Comparison of the mass transfer paths for the two cases is shown in Figure 4.5.1. It clearly indicates the expected trend of decreasing precipitation time with increasing relative humidity. The precipitation time for Case A2 is 192s while the precipitation time for Case A11 is 172s. However, the mass transfer path for Case A11 cuts the binodal curve at a relatively lower polymer concentration. Concentration profile of cellulose acetate at the moment of precipitation for the two cases in Figure 4.5.2 show less steep concentration gradient at the interface and larger difference between the top and bottom surfaces for Case A11 which has a higher relative humidity. This suggests the formation of more graded and porous membrane structure with a thinner skin layer for increasing relative humidity. Altinkaya et al. [10] also reported smaller percentages of dense skin layer with increasing relative humidity.

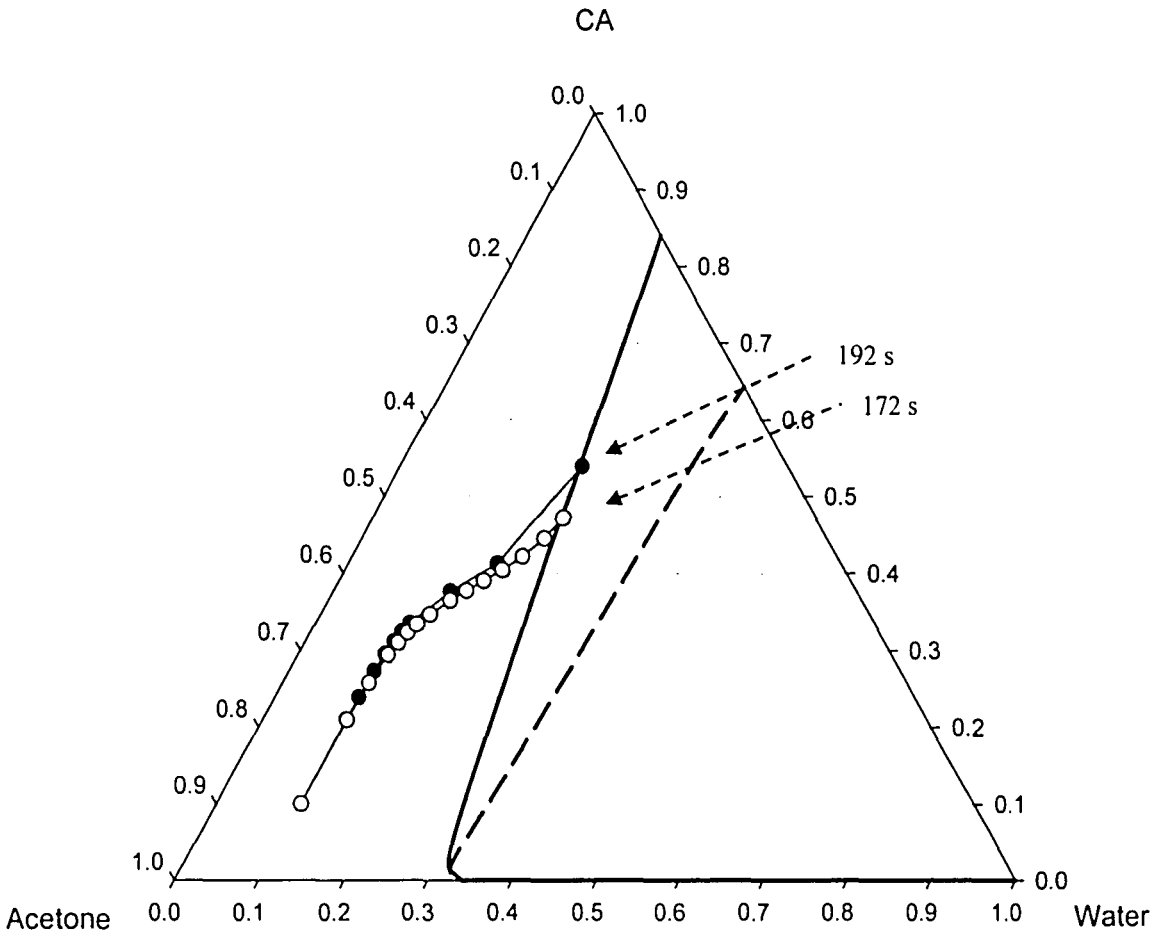

Figure 4.5.1: Mass transfer path of cellulose acetate, acetone and water at solution/air interface for two different air humidities given as cases A2 (●) and A11 (○) in Table 4.1.1.

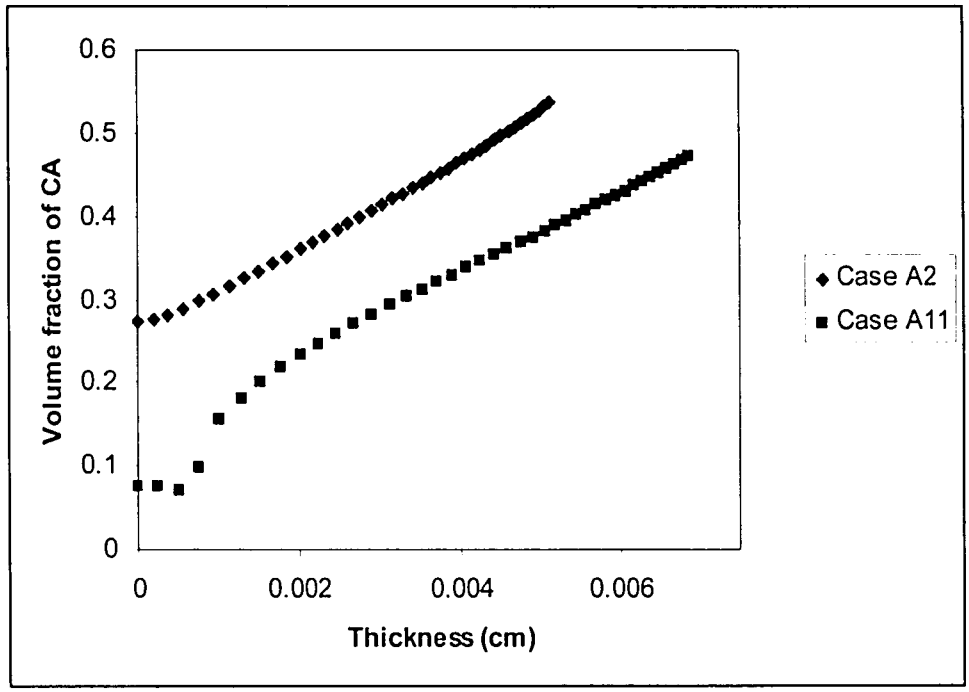

Figure 4.5.2: Concentration profile of cellulose acetate at the moment of precipitation for Cases A2 and A11.

4.6 The role of diffusion formalism

To illustrate the importance of the diffusion model on the phase separation kinetics in dry-casting, simulations corresponding to the input parameters denoted by Case A2 are performed for two alternative approximations of ternary diffusion coefficients. Figure 4.6.1 compares the two mass transfer paths for Case A2 where full diffusion coefficients or only main diffusion coefficients (the cross diffusion coefficients D_{12} and D_{21} are set to zero) are utilized. It is clearly seen that the two paths are very different from each other. The full diffusion model predicts a higher polymer concentration at phase separation and the precipitation time is longer. The concentration profiles of cellulose acetate at the moment of precipitation are also very different as indicated in Figure 4.6.2. The difference in concentration of CA at the two interfaces is

very large using the full diffusion model while the concentration profile of CA is almost flat using only main diffusion coefficients. A more asymmetric structure for the final film would be predicted without insertion of cross diffusion coefficients. The remarkable differences in the prediction of final film structure from different diffusion formalisms clearly point out the need for an accurate ternary diffusion model in dry-casting.

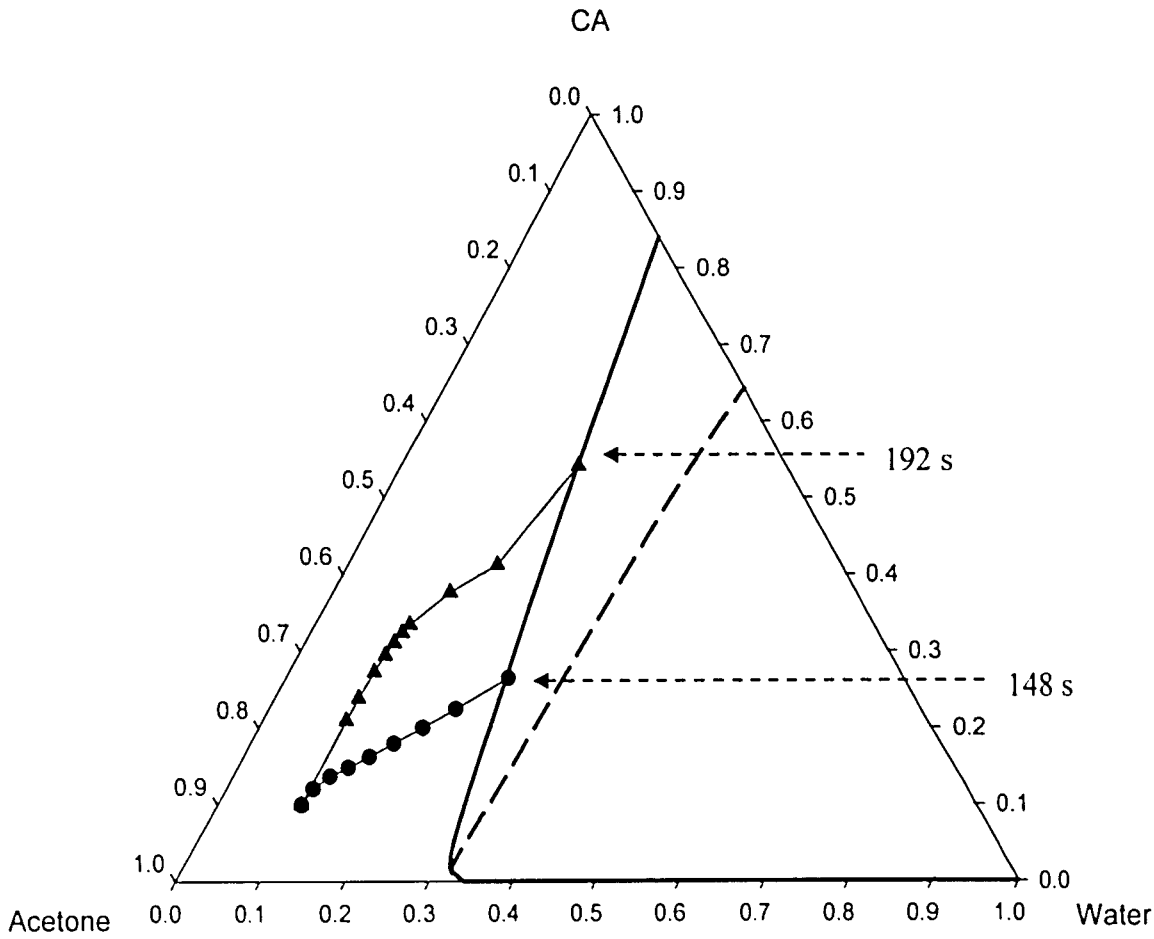

Figure 4.6.1: Mass transfer paths of CA, acetone and water at solution/air interface for Case A2 with full diffusion coefficients (▲) and $D_{12} = D_{21} = 0$ (●).

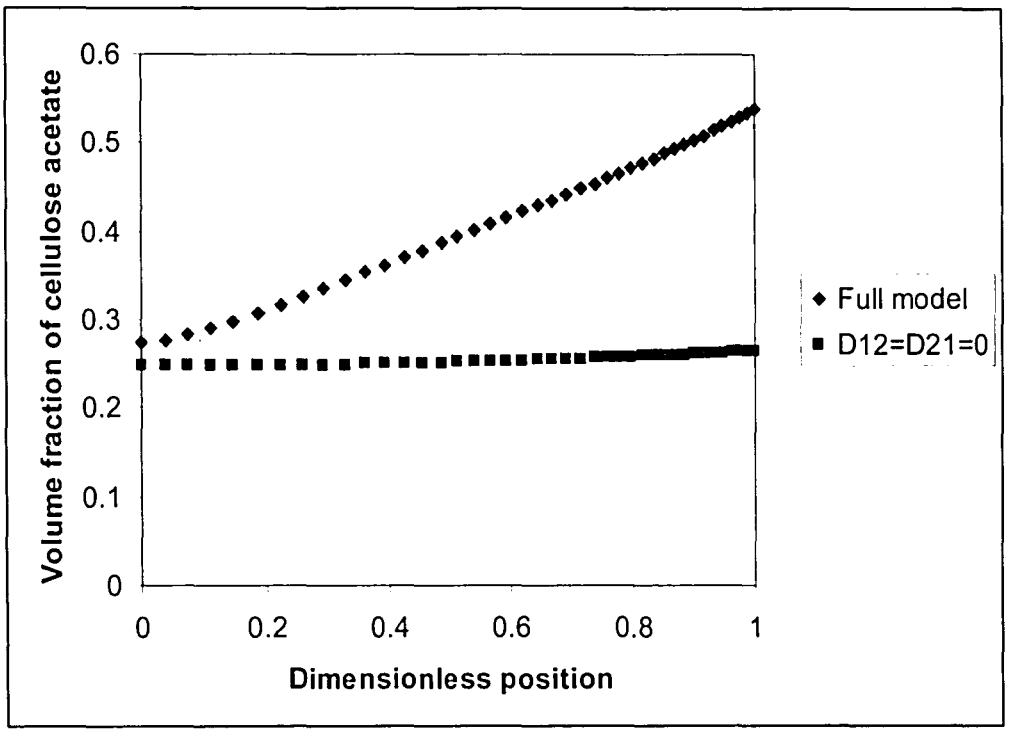

Figure 4.6.2: Concentration profile of cellulose acetate at the moment of precipitation for Case A2 with different diffusion formalisms.

Chapter 5

Results for Nonsolvent Vapor Induced Phase Separation

In most of this section, results are shown for the simulations of the cellulose acetate/acetone/water system to illustrate the effects of different operating conditions and the diffusion formalism on the predictions of the VIPS process. Model predictions for three other polymer systems are also made to validate the accuracy of the model through comparisons to experimental results reported in the literature. The input parameters used for the different simulations are shown in Table 5.1.1.

5.1 Effect of relative humidity

The relative humidity of the air plays an important role in the drying dynamics of the polymer film. In the process of VIPS where the initial casting solution contains solvent and polymer, increasing the relative humidity increases the driving force for a net diffusion into and accumulation of water in the film, thereby inducing phase separation. Therefore, relative humidity has a significant influence on the phase inversion kinetics and final membrane morphology in VIPS. Mass transfer paths that describe the solution-air interface composition and its variation with time can be superimposed onto the ternary phase diagram for morphological predictions.

Case	System	ϕ_i			T_0 (K)	T_g (K)	L (cm)	Relative humidity (%)	Mode of convection
		$i=1$	$i=2$	$i=3$					
A12	CA / acetone / water	0.00001	0.89999	0.1	296	297	0.02	51	Free
A13	CA / acetone / water	0.00001	0.89999	0.1	296	297	0.02	68	Free
A14	CA / acetone / water	0.00001	0.89999	0.1	296	297	0.02	98.5	Free
A15	CA / acetone / water	0.00001	0.89999	0.1	296	297	0.02	98.5	Forced, $u_\infty = 50$cm/s
A16	CA / acetone / water	0.00001	0.89999	0.1	296	297	0.02	98.5	Forced, $u_\infty = 200$cm/s
A17	CA / acetone / water	0.00001	0.89999	0.1	296	297	0.02	98.5	Forced, $u_\infty = 2000$cm/s
A18	CA / acetone / water	0.00001	0.89999	0.1	296	291	0.02	98.5	Free
A19	CA / acetone / water	0.00001	0.89999	0.1	296	285	0.02	98.5	Free
A20	CA / acetone / water	0.00001	0.89999	0.1	296	297	0.01	98.5	Free
A21	CA / acetone / water	0.00001	0.89999	0.1	296	297	0.04	98.5	Free
B1	PVDF / DMF / water	0.00001	0.94299	0.057	296	297	0.02	10	Free
B2	PVDF / DMF / water	0.00001	0.94299	0.057	296	297	0.02	20	Free
B3	PVDF / DMF / water	0.00001	0.94299	0.057	296	297	0.02	30	Free
B4	PVDF / DMF / water	0.00001	0.91259	0.0874	296	297	0.02	20	Free
B5	PVDF / DMF / water	0.00001	0.88049	0.1195	296	297	0.02	20	Free
C1	PSF / NMP / water	0.00001	0.87199	0.128	292.5	293	0.02	25	Free
C2	PSF / NMP / water	0.00001	0.87199	0.128	292.5	293	0.02	30	Free
C3	PSF / NMP / water	0.00001	0.87199	0.128	292.5	293	0.02	50	Free
D1	PEI / NMP / water	0.00001	0.86619	0.1338	312.5	313	0.025	25	Free
D2	PEI / NMP / water	0.00001	0.86619	0.1338	312.5	313	0.025	30	Free
D3	PEI / NMP / water	0.00001	0.86619	0.1338	312.5	313	0.025	60	Free

Table 5.1.1: Input parameters used for simulations in VIPS.

To investigate the effect of relative humidity in VIPS, three different relative humidities of 51%, 68% and 98.5% are compared with the initial volume fraction of water at essentially zero (0.00001). The simulations are denoted in Table 5.1.1 by Cases A12, A13 and A14, respectively for CA/acetone/water. All other input parameters are identical and are listed in Table 5.1.1. The mass transfer paths in Figure 5.1.1 show that phase separation is possible for relative humidities higher than about 68%, even for an initial casting solution containing no water. It also clearly indicates the expected trend of decreasing precipitation time with increasing relative humidity. The precipitation times are 207s and 151s for relative humidities of 68% and 98.5% respectively. During VIPS, there is water inflow into the film from the humid atmosphere and outflow of volatile acetone from the film by evaporation. As seen in Figure 5.1.2 where the water and acetone fluxes are illustrated for Case A14, the water flux at the interface is negative right up to 20s before the precipitation point, while the acetone flux at the interface is always positive. The water flux into the film increases rapidly in the beginning, reaches a plateau and then decreases until the fluxes of water and acetone are equal. There is eventually no driving force for water diffusing into the film because of its minimal concentration gradient across the film-air interface and it begins to evaporate form the system after 130s.

The effect of relative humidity in VIPS for systems with different miscibility gaps in the phase diagrams is illustrated for the PVDF/DMF/water, PS/NMP/water and PEI/ NMP/water systems which have much miscibility regions compared to the CA/acetone/water system. Since the binodal curve is very close to the polymer-solvent line, less water is required to diffuse into the film to induce phase separation.

For the PVDF/DMF/water system, three relative humidities of 10%, 20% and 30%, denoted by Cases B1, B2 and B3 are compared. All other input parameters are set the same as those reported by Matsuyama et al. [11] for comparison. The mass transfer paths in Figures 5.1.3, 5.1.4 and 5.1.5 show that phase separation occurs only for relative humidities higher than about 20% and the onset of phase separation occurs at 640s and 240s for relative humidities of 20% and 30% respectively. This agrees well with Matsuyama's experimental results [12] in which a change in membrane morphology from dense to porous structures was observed at a relative humidity of 20%.

For the PSF/NMP/water system, three relative humidities of 25%, 30% and 50% are compared and they are denoted by Cases C1, C2 and C3. The air temperature and initial polymer concentration are set the same as those reported by Park et al. [13]. The remaining parameters are listed in Table 5.1.1. Phase separation is not likely to occur for relative humidity below 25% since the induction time for precipitation is more than 24 hours from the model predictions. The mass transfer paths in Figures 5.1.6 and 5.1.7 show that phase separation occurs for relative humidities of 30% and 50% and the onsets of phase separation occur at 1120s and 480s respectively. Although Park et al. [13] reported that the critical humidity for phase separation was 65%, some of the operating conditions such as the initial film thickness and casting film surface area (L_c) were not stated. Changes in the film surface area will affect the mass transfer and heat transfer coefficients in Equations (3.4.1) and (3.4.8). Tsay and McHugh [23] illustrated the effect of casting film surface area on the mass transfer coefficient of acetone in a binary cellulose acetate/acetone system and concluded that the mass transfer coefficient and hence the evaporation rate increased with decreasing L_c. Shojaie et al. [6] also

commented that their model predictions for dry-casting were quite sensitive to the mass and heat transfer coefficients. Therefore, direct comparison to Park's experimental results cannot be applied here. However, our results show that the PSF/NMP/water system requires a much lower humidity for phase separation compared to the CA/acetone/water system under the same operating conditions. Moreover, the similar mass transfer paths for the two different relative humidities in Figures 5.1.6 and 5.1.7 suggest that increasing relative humidity only changes the precipitation time but not the final film morphology for this system.

For the PEI/NMP/water system, three relative humidities of 25%, 30% and 70% denoted by Cases D1, D2 and D3 are compared. All the other input parameters are the same as those reported by Caquineau et al. [15] for comparison. Phase separation is not likely to occur for relative humidity below 25% since the induction time for precipitation is more than 24 hours from the model predictions. The mass transfer paths in Figures 5.1.8 and 5.1.9 show that phase separation occurs for relative humidity higher than 30% and the onsets of phase separation occur at 3.5hr and 281s for relative humidities of 30% and 70% respectively. This agrees reasonably well with Caquineau's experimental results. He reported that above a relative humidity of 27%, the films presented a cell-like structure.

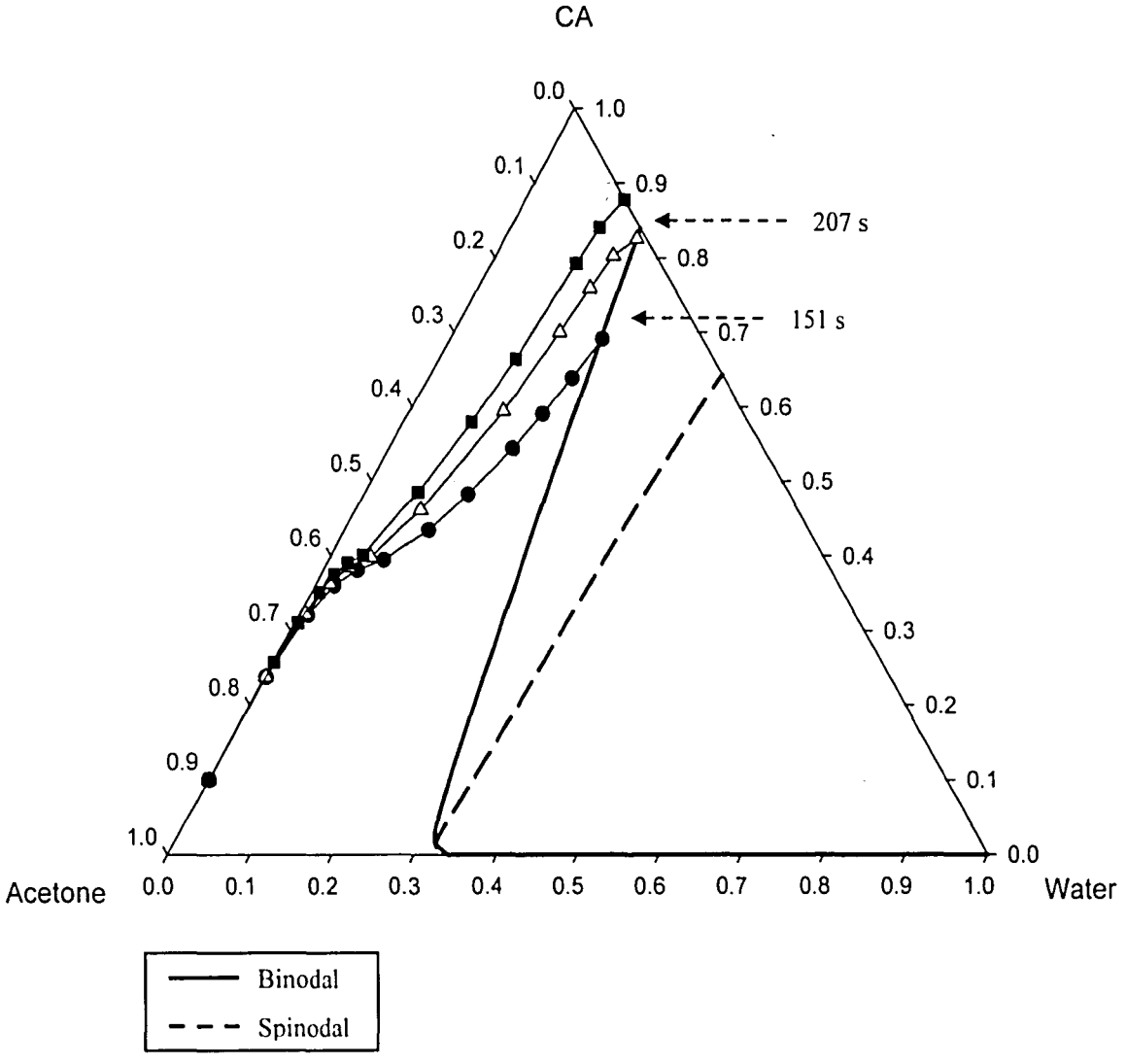

Figure 5.1.1: Mass transfer path of cellulose acetate, acetone and water at solution/air interface for various air relative humidities listed as cases A12 (■), A13 (△) and A14 (●) in Table 5.1.1.

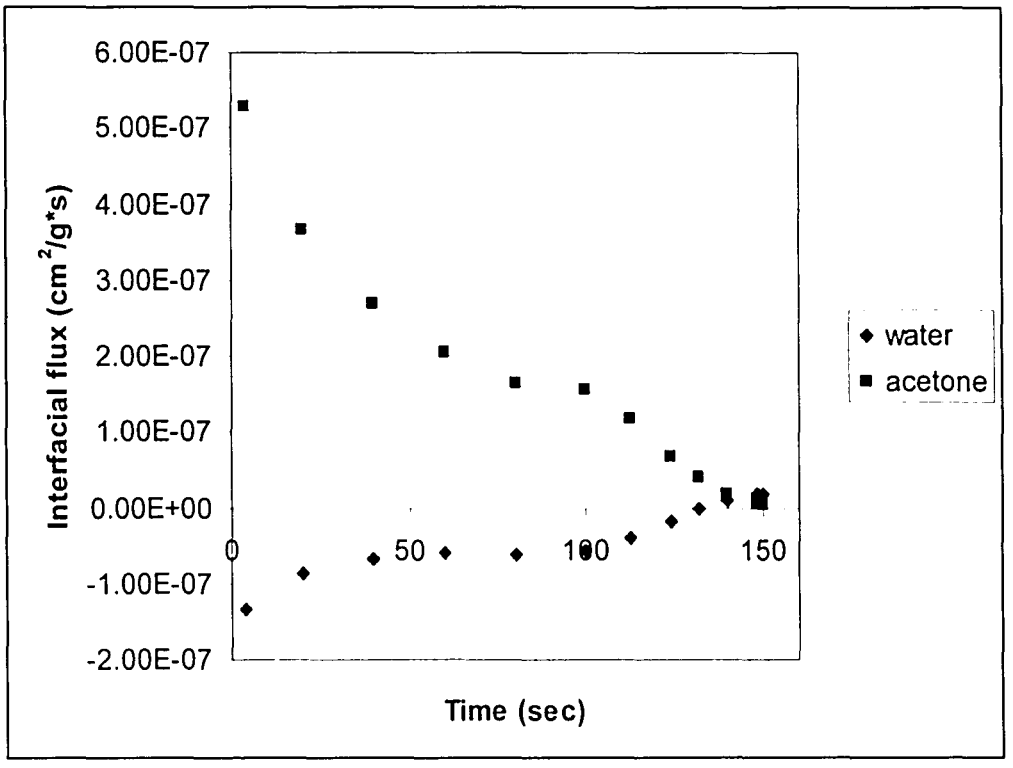

Figure 5.1.2: The fluxes of water and acetone at interface for Case A14.

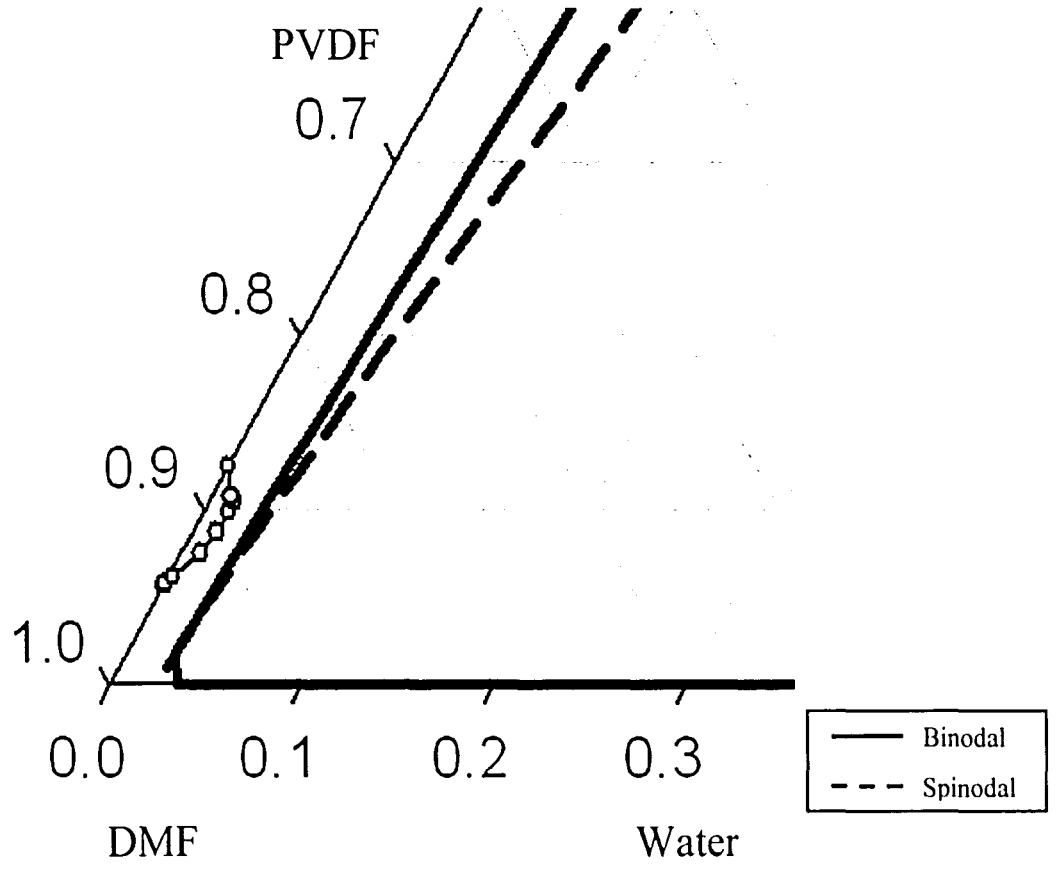

Figure 5.1.3: Mass transfer path of PVDF, DMF and water at solution/air interface for Case B1.

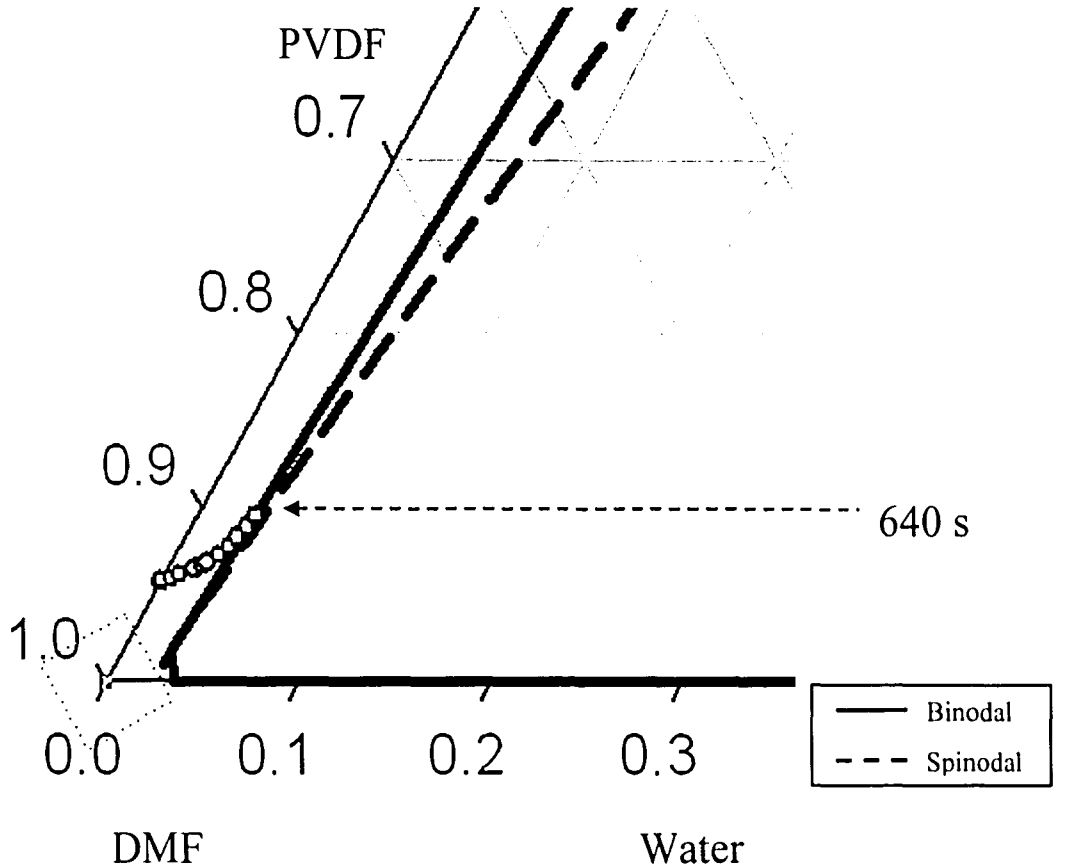

Figure 5.1.4: Mass transfer path of PVDF, DMF and water at solution/air interface for Case B2.

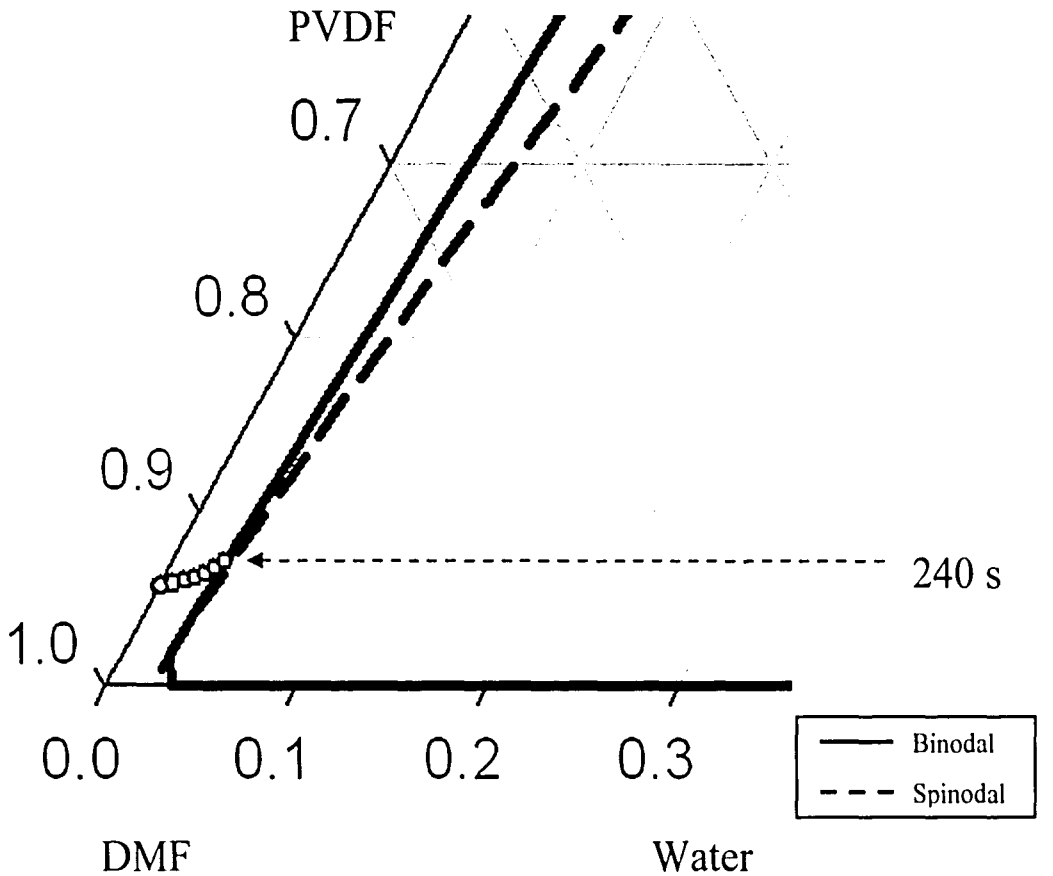

Figure 5.1.5: Mass transfer path of PVDF, DMF and water at solution/air interface for Case B3.

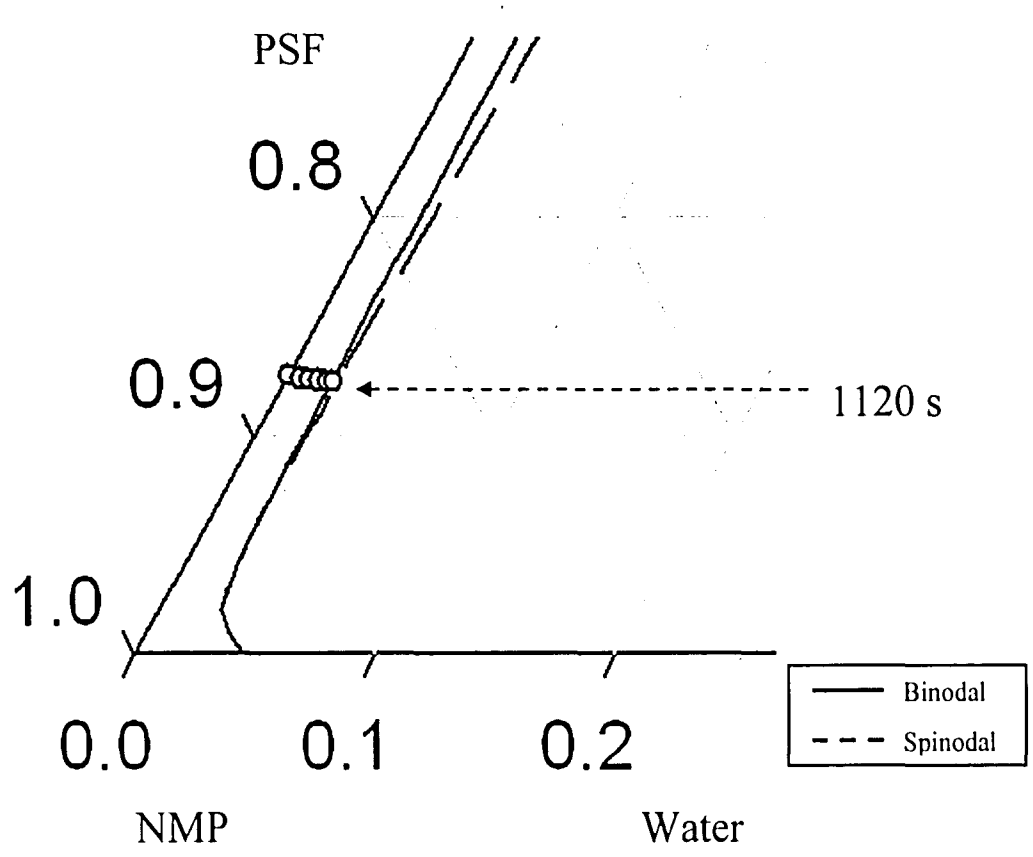

Figure 5.1.6: Mass transfer path of PSF, NMP and water at solution/air interface for Case C2.

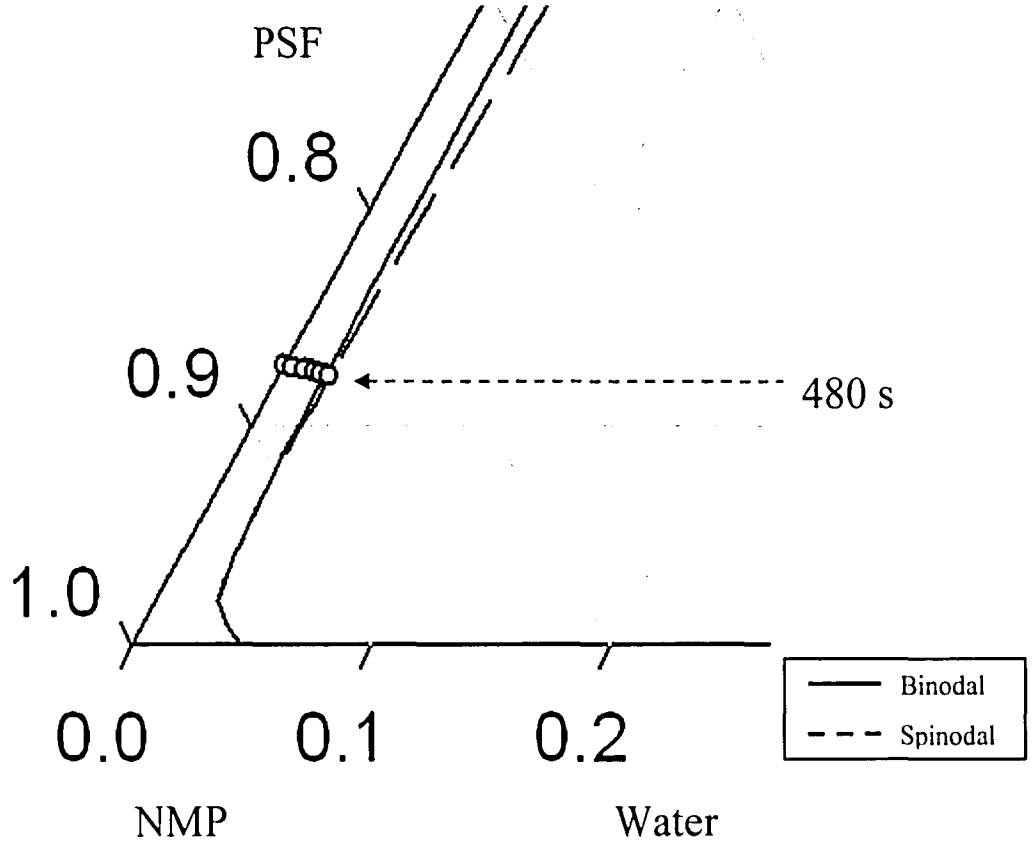

Figure 5.1.7: Mass transfer path of PSF, NMP and water at solution/air interface for Case C3.

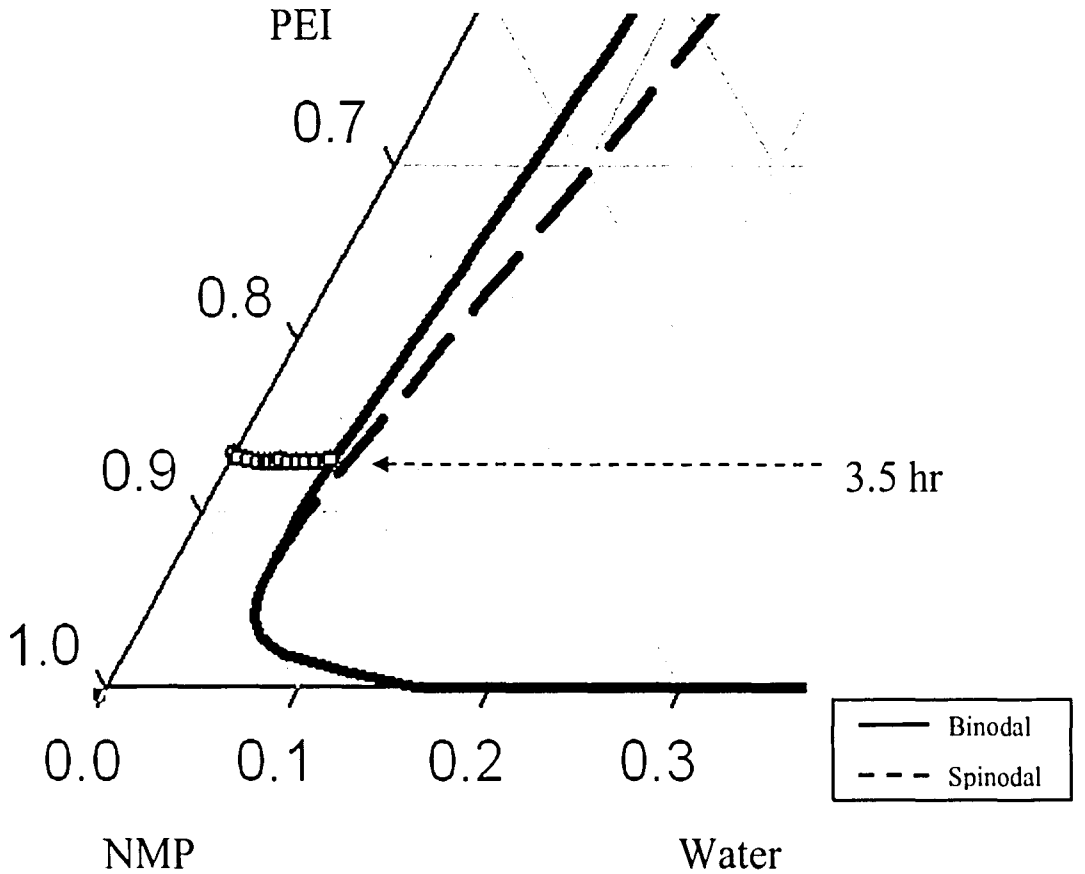

Figure 5.1.8: Mass transfer path of PEI, NMP and water at solution/air interface for Case D2.

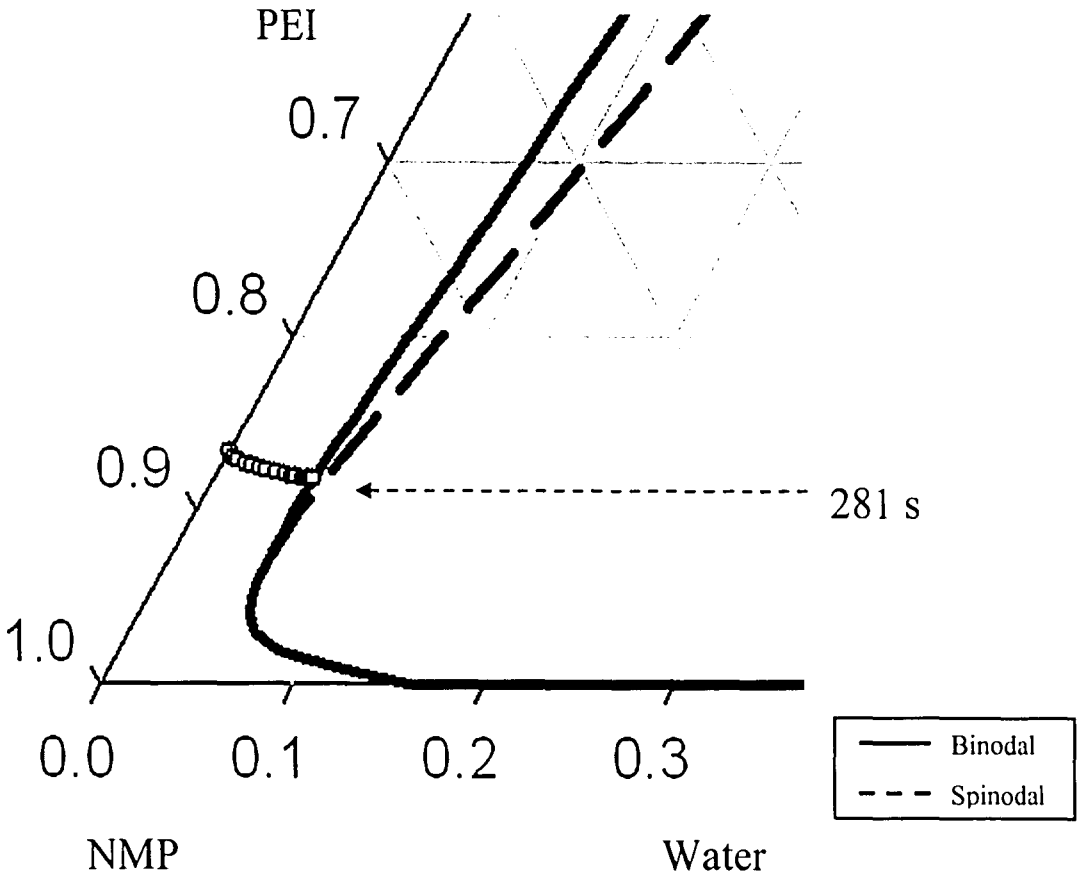

Figure 5.1.9: Mass transfer path of PEI, NMP and water at solution/air interface for Case D3.

5.2 Effect of solvent volatility

Solvent volatility affects the evaporation rate and hence the concentration of water in the polymer film. To investigate this effect, systems with solvents of different volatility are compared. Due to the high boiling points of DMF (153°C) and NMP (202°C) compared to acetone (56.5°C), the evaporation of solvents in PVDF/DMF and PSF/NMP systems is negligible compared to that in the CA/acetone system. During VIPS, the PVDF/DMF and PSF/NMP systems continue to absorb water vapor from the humid atmosphere and there is almost no solvent loss to the surrounding. Therefore, unlike the

CA/acetone system, the PVDF/DMF and PSF/NMP systems exhibit a slight increase in the overall film thickness. This prediction is demonstrated in Figure 5.2.1 which shows the thickness profile for the three different systems at their critical humidities, denoted by Cases A13, B2 and C2. On the other hand, it should be noted that Matsuyama et al. [11] predicted 80% film shrinkage for the PVDF/DMF/water system. The reason for their prediction probably arises from their assumption of quasi-binary assumption and setting D_{21} to zero in their model. This emphasizes the importance of incorporating complete multicomponent diffusivities in VIPS. Although the initial casting solution is binary, and the volume fraction of water is fairly lower than that of solvent during exposure to humid air, the amount of water diffusing into the film is critical in determining phase transition. Hence the diffusion coefficient D_{21} cannot be neglected.

The evaporative cooling effects for the PVDF/DMF and PSF/NMP systems are also minimal compared to the CA/acetone system because of slow evaporation of solvent. As indicated in Figure 5.2.2, which shows the temperature profile for the three different systems at their critical humidities (denoted by Cases A13, B2 and C2), temperature remains almost constant for the PVDF/DMF and PSF/NMP systems while it shows a decrease of 5K for the CA/acetone system. Therefore, the assumption of isothermal process is not appropriate for rapid-evaporating systems.

In VIPS, the concentration profile at the moment of precipitation for different systems varies which reflects the possibility of different phase separation dynamics and morphology development in the precipitated film. As shown in Figures 5.2.3, 5.2.4 and 5.2.5, the concentration profiles of the nonsolvent, solvent and polymer across the film are relatively flat for systems having low volatile solvents. Therefore, a symmetric

instead of asymmetric morphology is predicted for these systems in VIPS. Similar observations were also reported by Park et al. [13]. Although membranes made by the wet cast process in general exhibit an asymmetric structure, those produced by VIPS can have structures ranging from symmetric to asymmetric depending on the systems and solvents used.

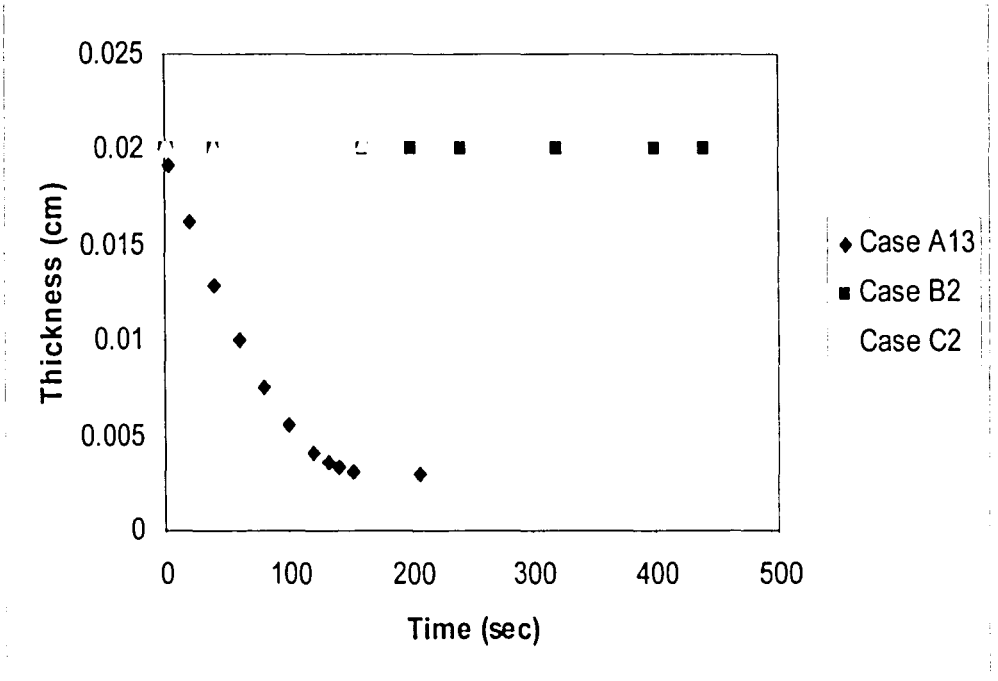

Figure 5.2.1: Thickness change as a function of time for Cases A13, B2 and C2.

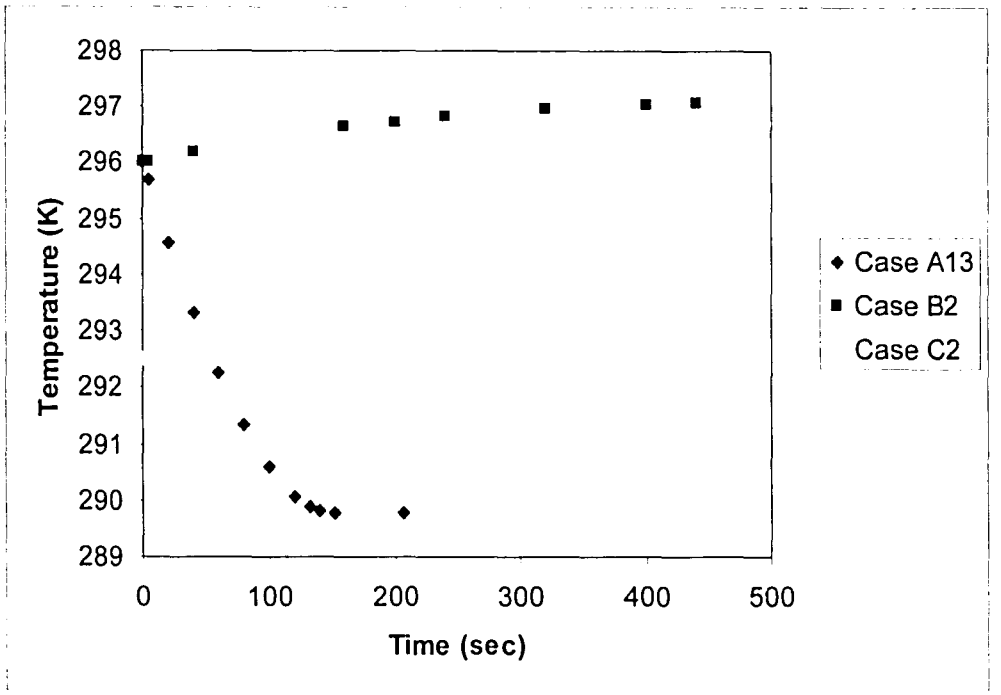

Figure 5.2.2: Temperature change as a function of time for Cases A13, B2 and C2.

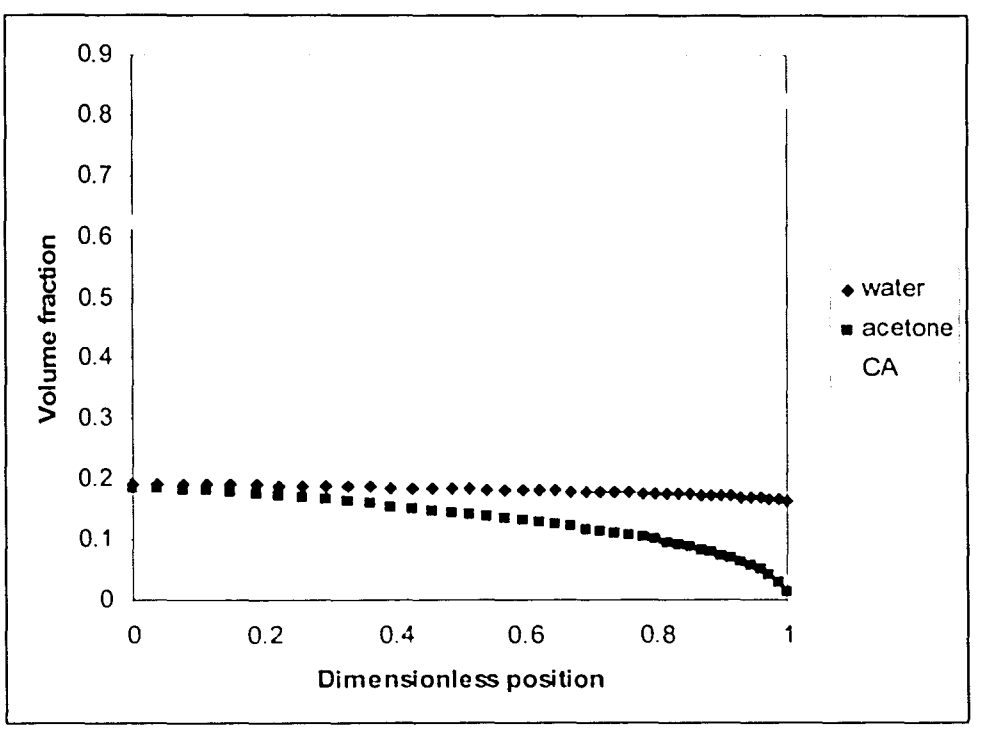

Figure 5.2.3: Concentration profiles of water, acetone and cellulose acetate at the moment of precipitation for Case A13.

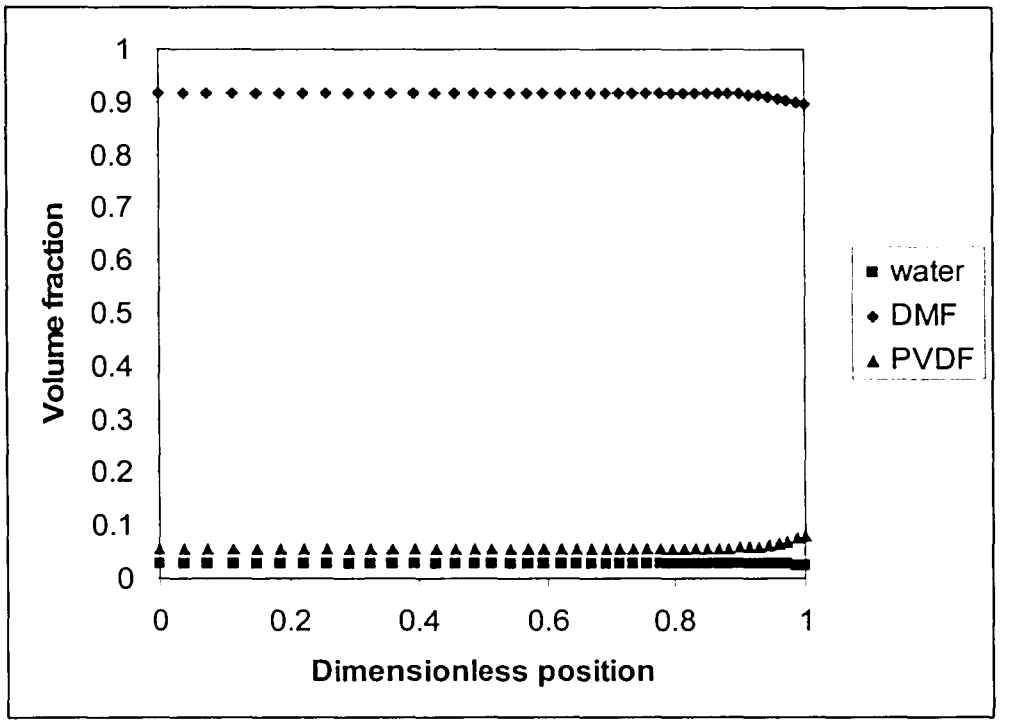

Figure 5.2.4: Concentration profiles of water, DMF and PVDF at the moment of precipitation for Case B2.

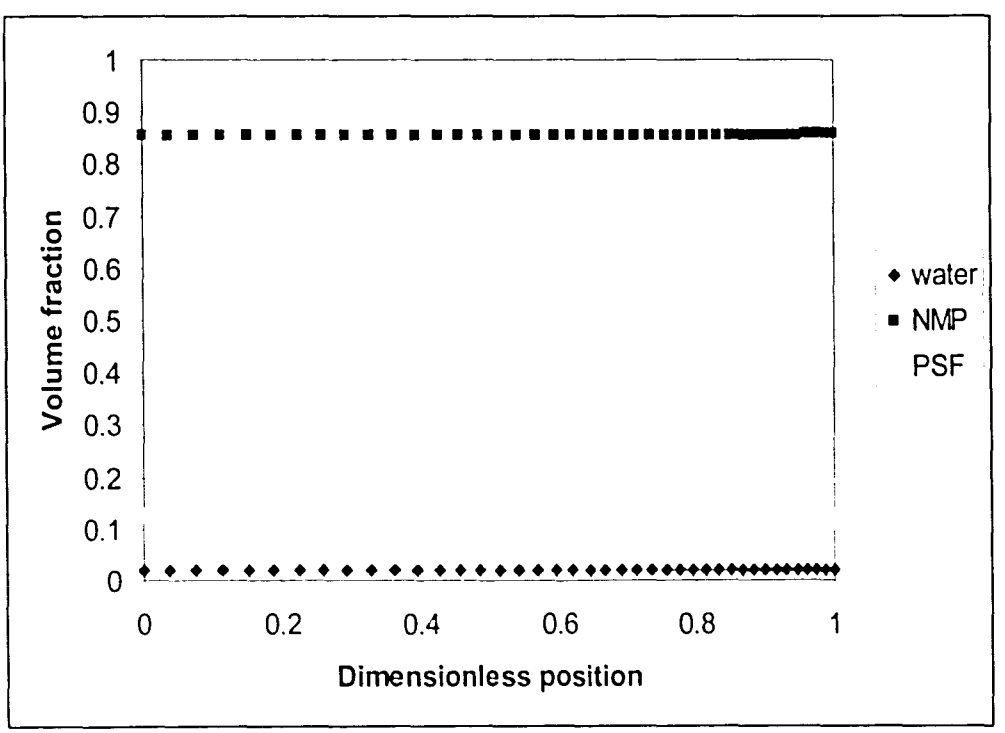

Figure 5.2.5: Concentration profiles of water, NMP and PSF at the moment of precipitation for Case C2.

5.3 Effect of evaporation conditions

In drying of polymer films, the evaporation of solvent to the gas phase can be controlled either by free convection or forced convection processes. To investigate the effect of evaporation conditions in VIPS, three simulations with different air velocities were performed. They are denoted by Cases A15, A16 and A17 in which the air velocities are 50cm/s, 200cm/s and 2000cm/s, respectively, while all the other input parameters are kept the same as those in Case A14. Comparison of the mass transfer paths for these three cases is shown in Figure 5.3.1. It is seen that increasing the air velocity favors phase separation and increases the evaporation rate. The precipitation times for Cases A15, A16 and A17 are 60s, 32s and 19s respectively, compared to the precipitation time of 151s for Case A14 where VIPS is carried under free convection.

Contrary to the dry-casting process in which the initial casting solution contains water [9], phase separation will not be completely suppressed in VIPS even with an air velocity as high as 2000cm/s. However, the different mass transfer paths for different air velocities suggest different film morphologies. Polymer concentration profiles for Cases A15, A16 and A17 in Figure 5.3.2 plotted against position in the film to better illustrate behavior patterns that could be used to predict film morphology. One sees that with increased air velocity, the following features are exhibited: (1) film shrinkage will be decreased due to decreased precipitation time; (2) formation of thicker skin, particularly for case A17, will be favored, while cases A15 and A16 should exhibit similar skin thicknesses; (3) formation of graded-pore sublayer structures will be favored, and be most pronounced for case A17.

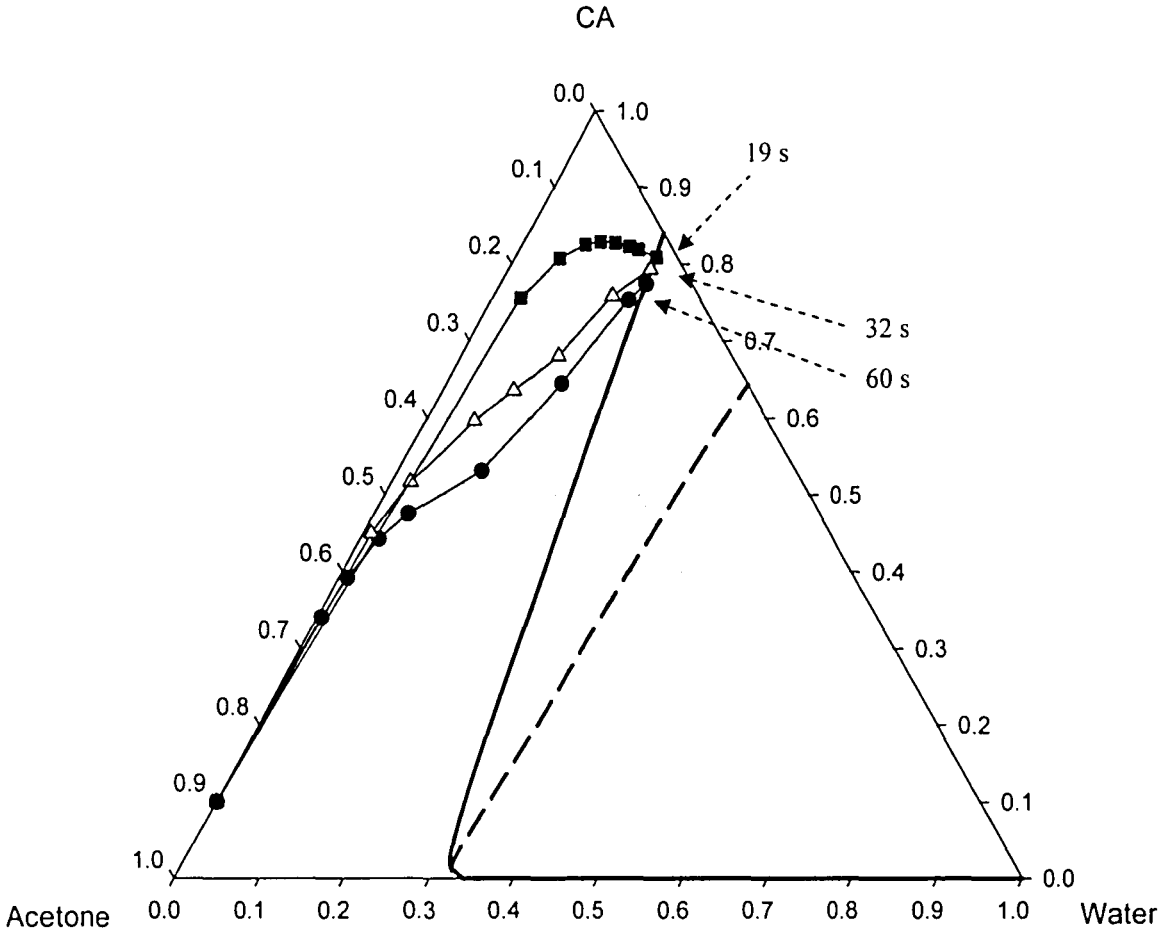

Figure 5.3.1: Mass transfer path of cellulose acetate, acetone, water at solution/air interface for three different air velocities listed as Cases A15 (●), A16 (△) and A17 (■) in Table 5.1.1.

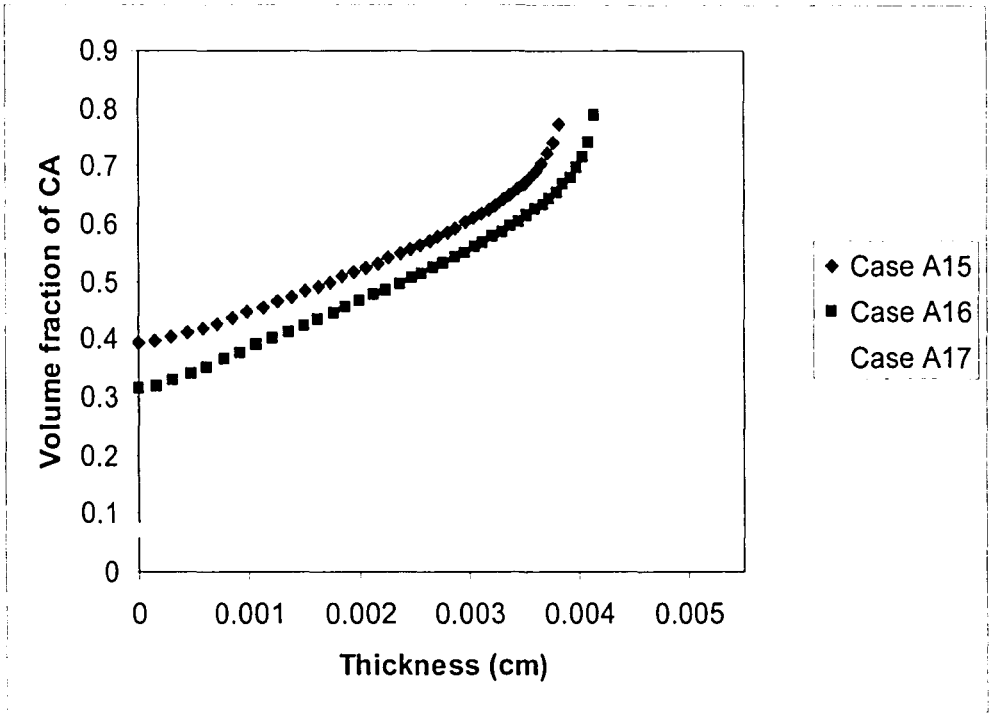

Figure 5.3.2: Concentration profile of cellulose acetate at the moment of precipitation for Cases A15, A16 and A17.

5.4 Effect of evaporation temperature

The effect of evaporation temperature is investigated by comparing three different air temperatures at 285K, 291K and 297K. The simulations are denoted by Cases A14, A18 and A19 respectively. All the other input parameters for Cases A18 and A19 are identical to those of Case A14. As expected, decreasing the air temperature leads to slower evaporation of acetone from the solution-air interface and decreased water concentration inside the film. The results show the expected trend of increasing precipitation time with decreasing air temperature in Figure 5.4.1. The precipitation time for Case A14 is 151s while the precipitation time for Case A18 is 206s. It is also seen that phase separation is not possible for air temperature lower than 291K with the input

parameters listed as Case A19. Thus for these conditions a uniformly dense structure should result.

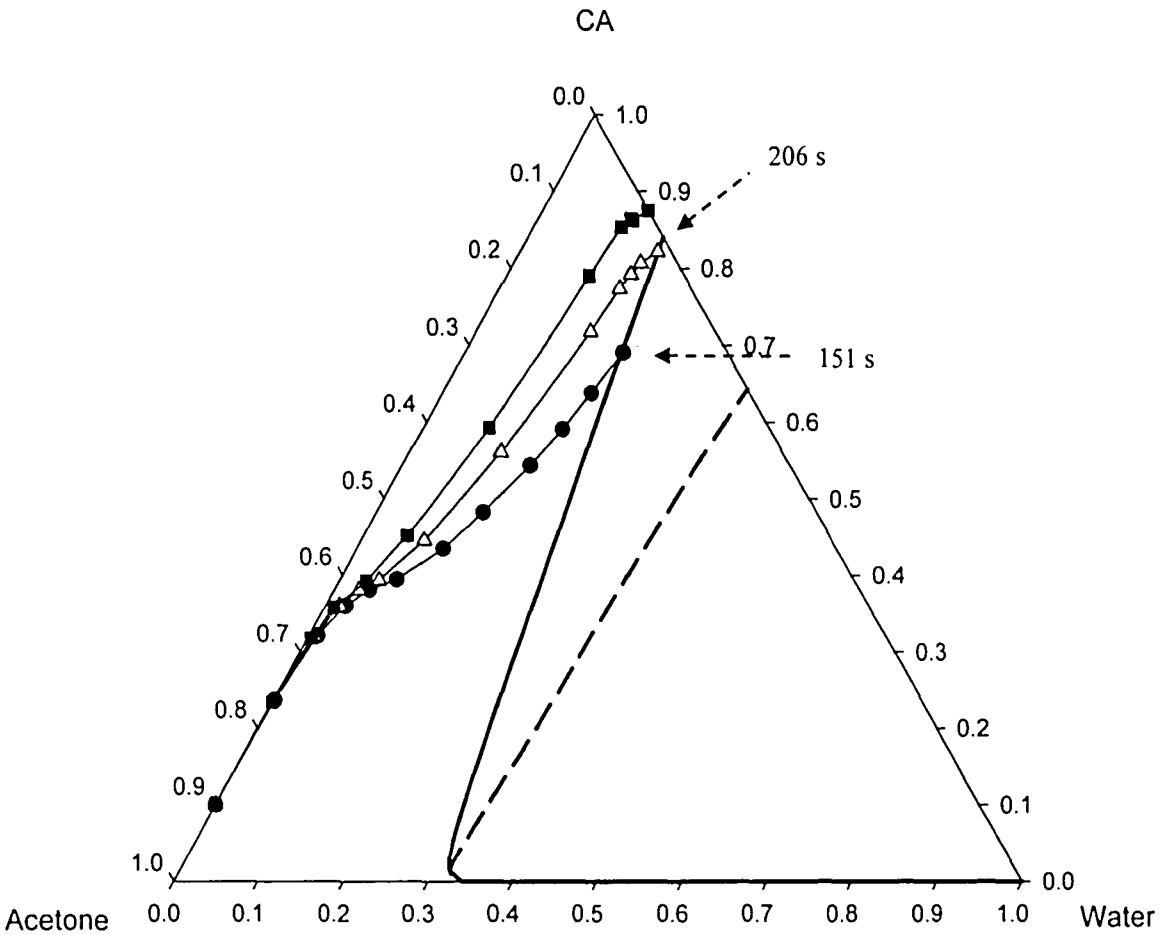

Figure 5.4.1: Mass transfer path of cellulose acetate, acetone and water at solution/air interface for three different air temperatures listed as cases A18 (■), A19 (△) and A14 (●) in Table 5.1.1.

5.5 Effect of initial film thickness

To investigate the effect of initial film thickness of the casting solution, three different initial film thicknesses of 0.01cm, 0.02cm and 0.04cm are compared. The simulations are denoted by Cases A20, A14 and A21 respectively. All the other input parameters for Cases A20 and A21 are identical to those of Case A14. As can be seen from Figure 5.5.1, the three mass transfer paths intercept the binodal curve at the same interfacial concentration. The corresponding precipitation times for Cases A20, A14 and A21 are 70s, 151s and 346s respectively. Decreasing initial film thickness leads to decreasing precipitation time, hence faster phase separation. While the final polymer concentrations at the moment of precipitation are the same for the three cases, the mass transfer paths and hence the concentration profiles of the three components are different. Polymer concentration profiles for Cases A20, A14 and A21 in Figure 5.5.2 indicate that the polymer concentration gradient increases with increasing initial film thickness. Therefore, a less dense structure with graded-pore sublayer would be predicted for Case A21.

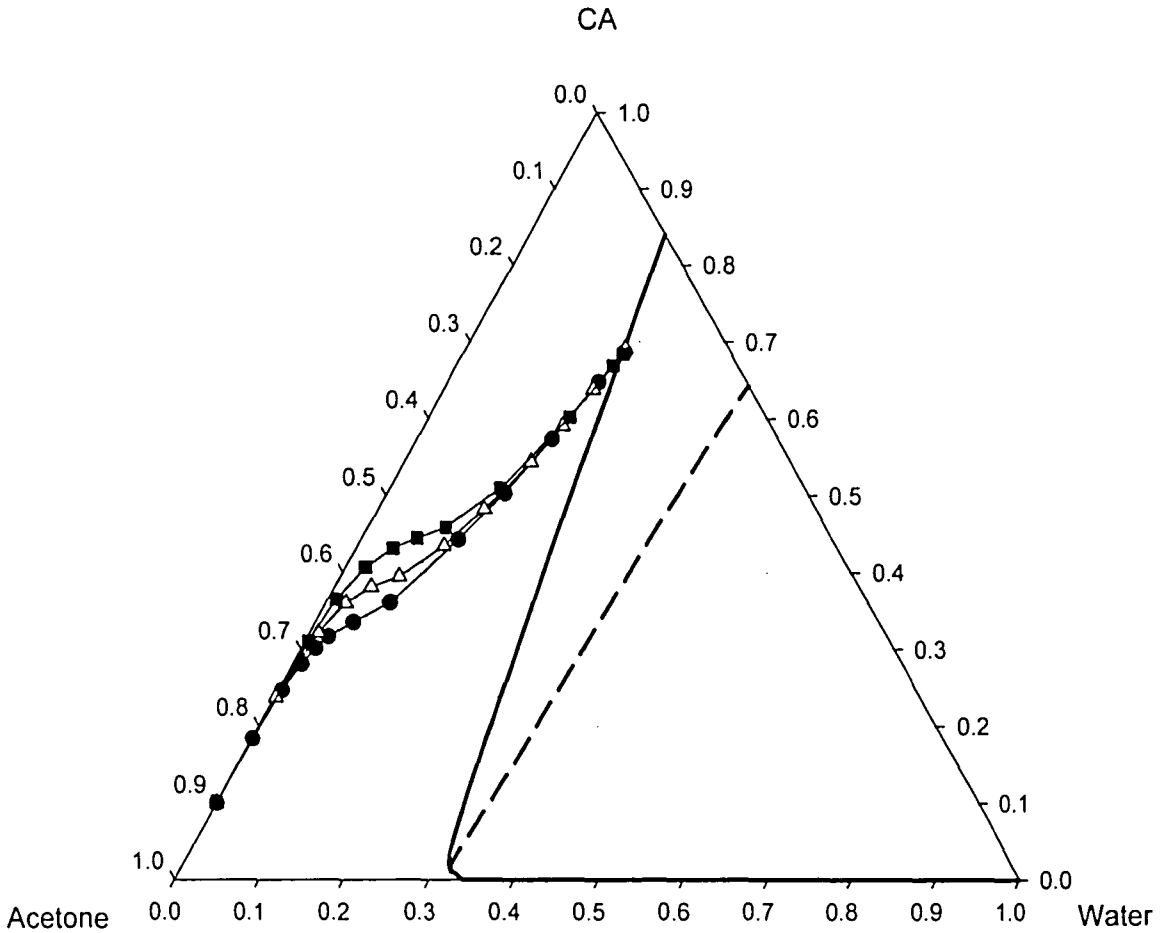

Figure 5.5.1: Mass transfer path of cellulose acetate, acetone and water at solution/air interface for three different film thicknesses listed as cases A20 (■), A14 (△) and A21 (●) in Table 5.1.1.

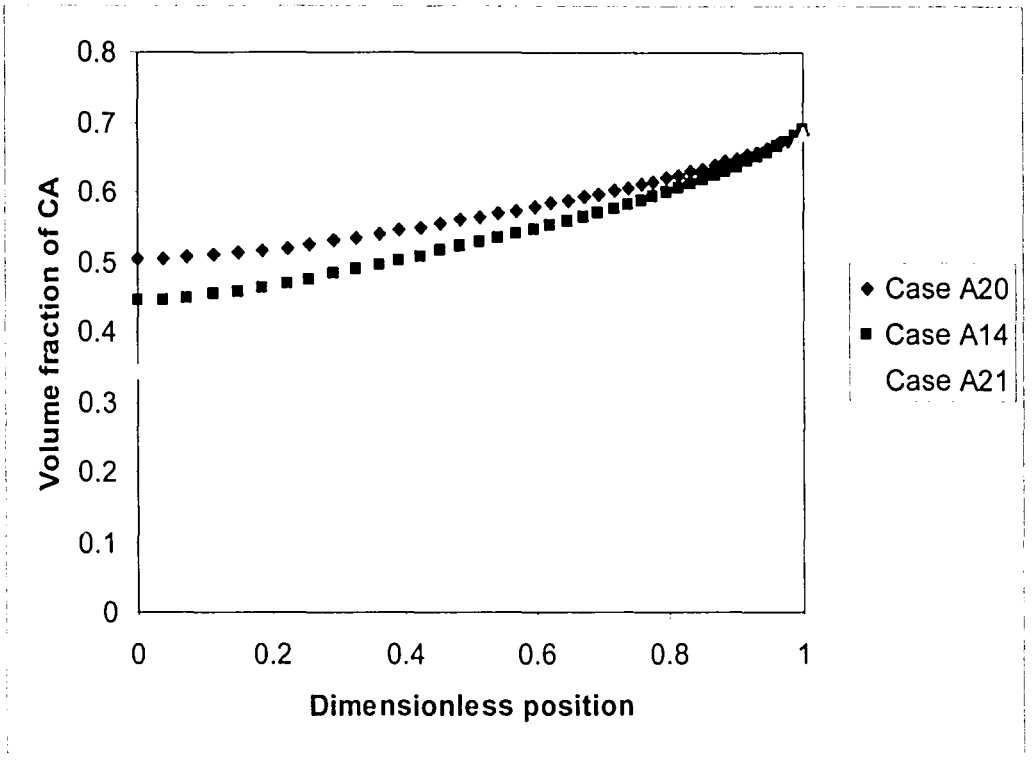

Figure 5.5.2: Concentration profile of cellulose acetate at the moment of precipitation for Cases A20, A14 and A21.

5.6 Effect of initial polymer concentration

The effect of initial polymer concentration in the casting solution was investigated with the PVDF/NMP/water system for comparison with the experimental results of Matsuyama et al. [12]. Three different polymer volume fractions of 0.057, 0.0874 and 0.1195 (corresponding to weight percents of 10%, 15% and 20%) are compared. The simulations are denoted by Cases B2, B4 and B5 respectively. All the other input parameters are set the same as those reported by Matsuyama et al. As indicated in Figures 5.1.4, 5.6.1 and 5.6.2, increasing initial polymer concentration causes the mass transfer path to intercept the binodal curve at a higher polymer concentration and at a longer time.

The precipitation times for Cases B2, B4 and B5 are 640s, 720s and 1120s respectively. Since the final film contains higher polymer concentration, a less porous structure would be predicted for Cases B4 and B5. This agrees well with Matsuyama's experimental results which show less pores for the films cast from higher polymer concentration solutions.

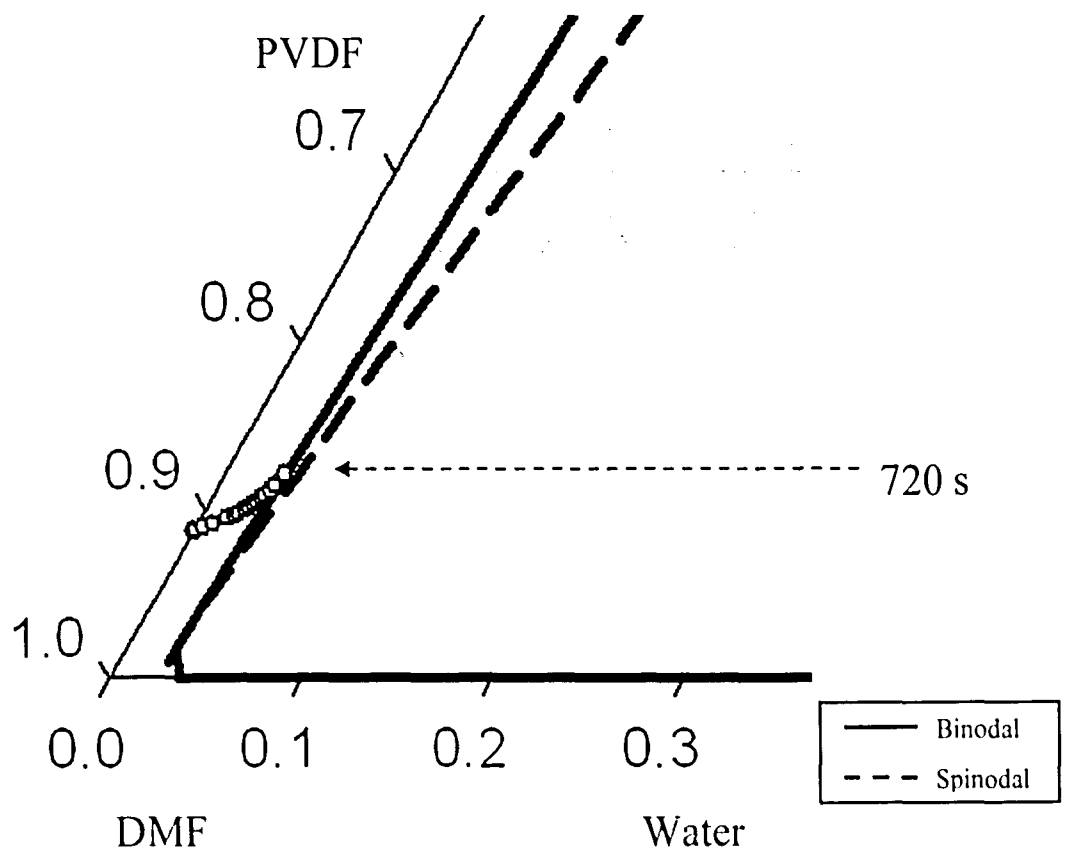

Figure 5.6.1: Mass transfer path of PVDF, DMF and water at solution/air interface for Case B4.

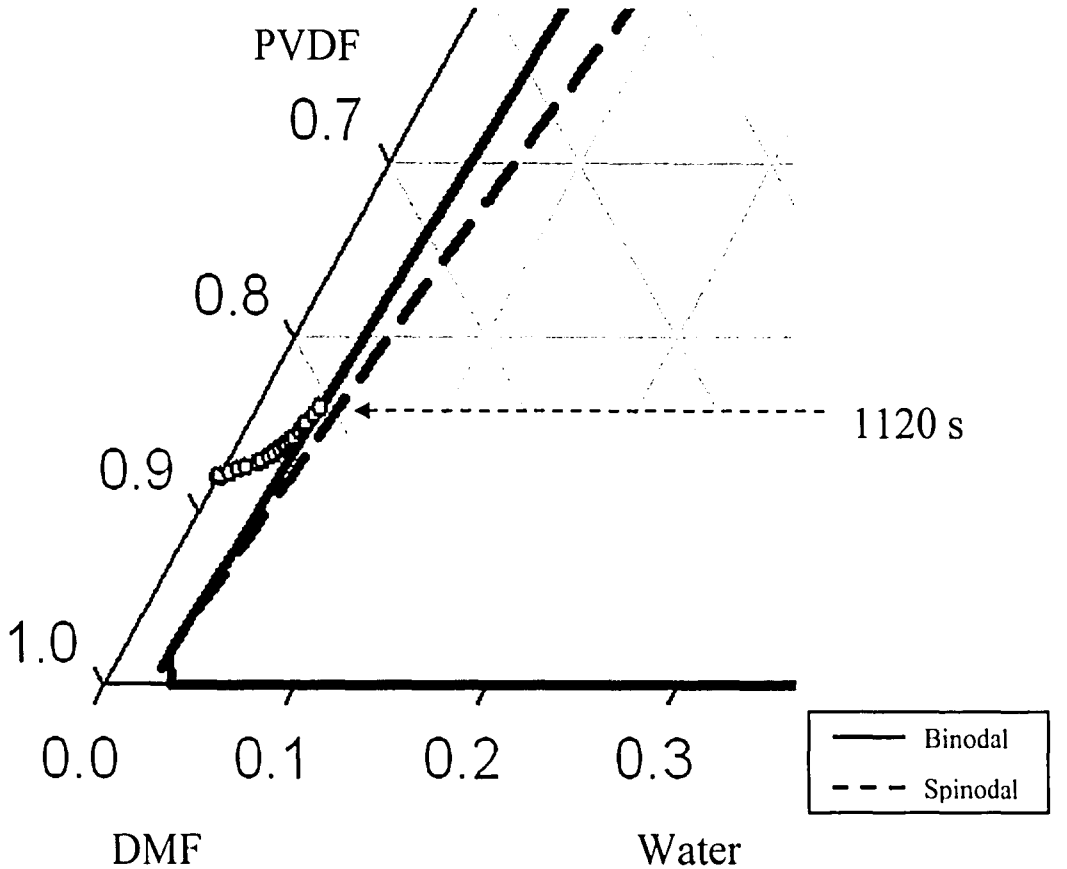

Figure 5.6.2: Mass transfer path of PVDF, DMF and water at solution/air interface for Case B5.

5.7 The role of diffusion formalism

To illustrate the importance of the diffusion model on the phase separation kinetics in VIPS, simulations corresponding to the input parameters denoted by Case A14 were performed for two alternative approximations of ternary diffusion coefficients. One approximation of the diffusion model is setting D_{21} to zero, as suggested by Matsuyama et al. [11]. Figure 5.7.1 compares the two mass transfer paths for Case A14 where the complete ternary diffusion coefficient formalism was used and the partial diffusion coefficients (D_{11}, D_{12}, D_{22}) are utilized. The full diffusion model predicts a higher

polymer concentration at phase separation and a longer precipitation time. It is also interesting to note that the acetone concentration at the interface decreases initially and then remains constant for a short period of time with the partial diffusion coefficient model. Shojaie et al. [5] explained this effect as a marked decrease in the rate of acetone loss. The free surface concentration of acetone remains constant while the bulk concentration is decreasing at some point of phase separation process. The concentration profiles of cellulose acetate at the moment of precipitation are also very different as indicated in Figure 5.7.2. The difference in concentration of CA at the two interfaces is very large using the full diffusion model while the concentration profile of CA is almost flat using only partial diffusion coefficients. A more asymmetric structure for the final film would be predicted without insertion of D_{21}. The remarkable differences in the prediction of final film structure from different diffusion formalisms clearly point out the need for an accurate ternary diffusion model in VIPS.

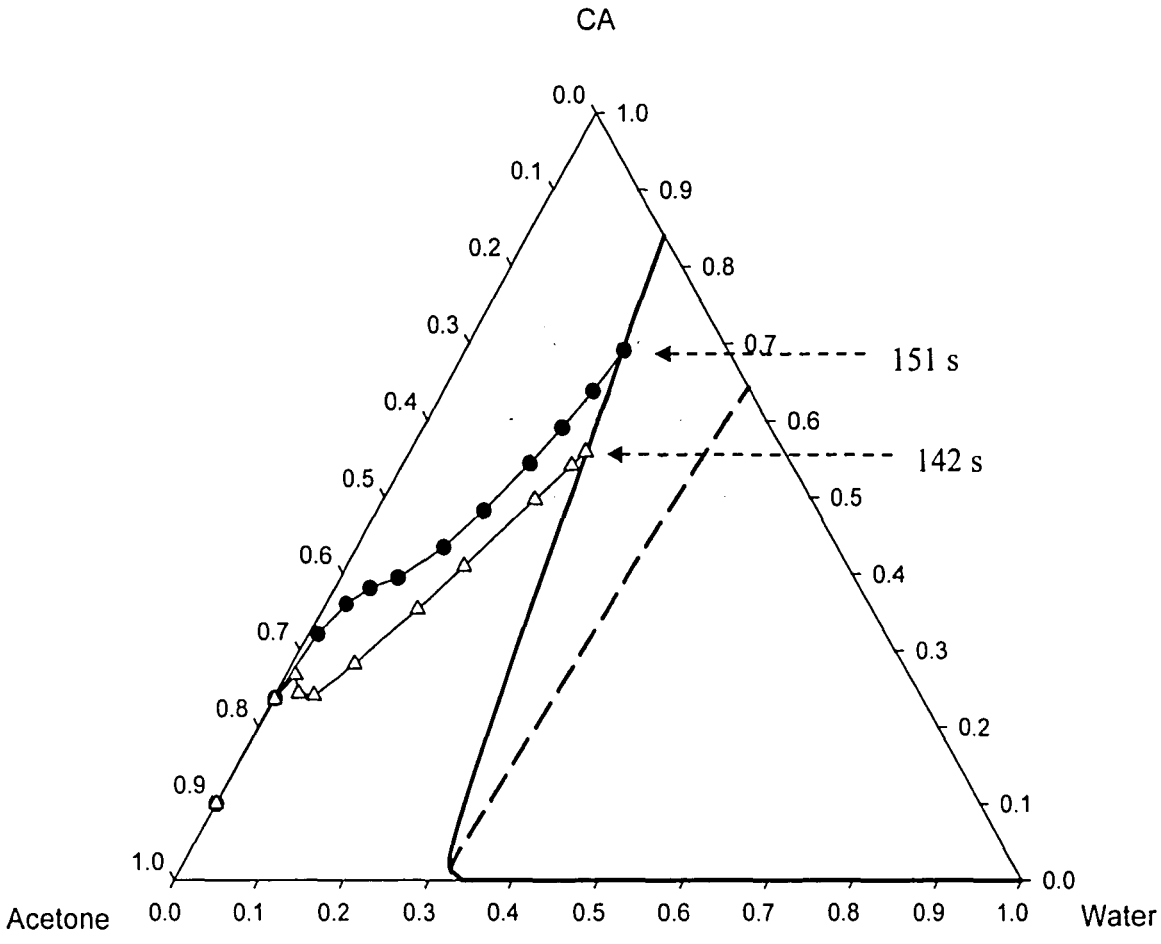

Figure 5.7.1: Mass transfer paths of CA, acetone and water at solution/air interface for Case A14 with full diffusion coefficients (●) and $D_{21} = 0$ (△).

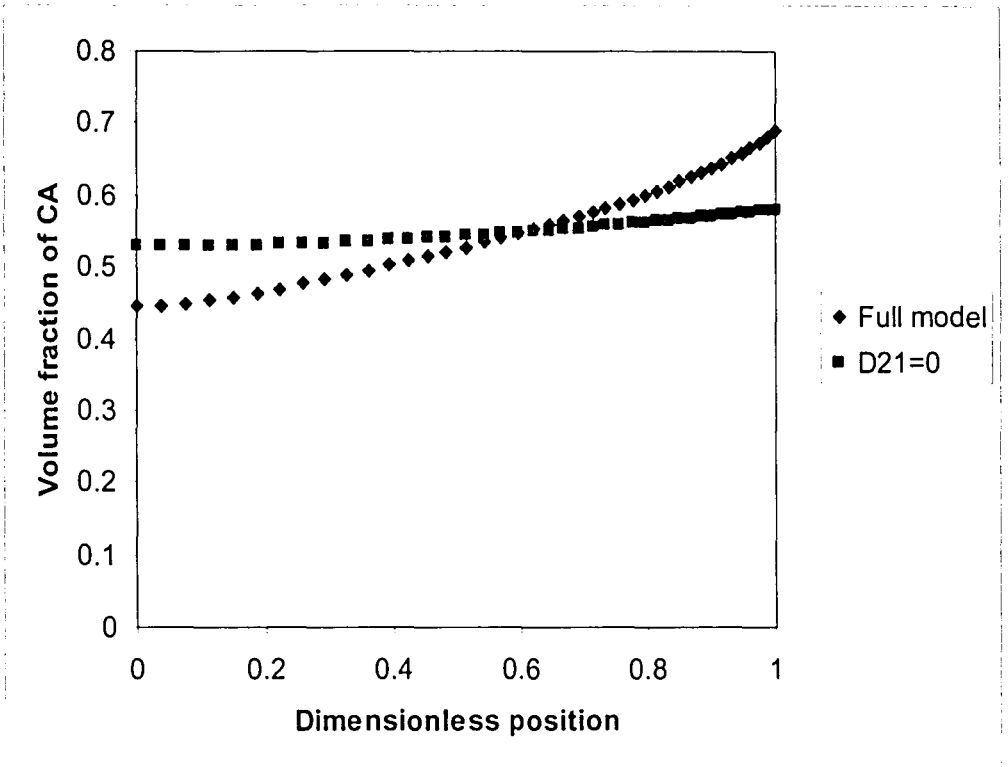

Figure 5.7.2: Concentration profile of cellulose acetate at the moment of precipitation for Case A14 with different diffusion formalisms.

Chapter 6

Conclusions

In this study, a drying model for predicting the mass transfer path on phase diagram and hence the final membrane structure is implemented for both dry-casting and nonsolvent vapor induced phase separation. The model captures the important thermodynamic and kinetic phenomena and its predictions agree well with most experimental results in the literature. Model predictions indicate that the initial nonsolvent/polymer concentration, initial film thickness, evaporation temperature, evaporation condition and relative humidity all have substantial influences on the final film structure for both dry-casting and VIPS.

In dry-casting, there is a minimum amount of water required in the initial casting solution to induce phase separation for evaporation of solvent/nonsolvent under dry atmosphere. It is possible to change the membrane morphology from dense to porous structure by increasing initial nonsolvent concentration in casting solution. Increasing air temperature and decreasing initial film thickness lead to faster phase separation and hence decreasing precipitation time. Phase separation can also be completely suppressed with increasing air velocity. Increased relative humidity favors the formation of graded and porous structures with less dense skin layers.

In VIPS, phase separation is possible for relative humidity higher than a critical value even for an initial casting solution containing no water (nonsolvent). The minimum or critical humidity required to induce phase separation varies with different polymer-solvent systems. The critical humidity is lower for systems having large miscibility gaps in the phase diagram. Membranes made from slow-evaporating systems, i.e. using high boiling point solvents, usually exhibit a symmetric rather than an asymmetric morphology. It is also possible to change the membrane morphology from a dense to porous structure by increasing the evaporation temperature. Increased air velocity and initial film thickness favor the formation of graded-pore structures and dense skins. Increasing the initial polymer concentration and thus decreasing initial solvent concentration decreases water inflow from the gas phase and increases precipitation time.

It was also found that full diffusion theory is important in accurate prediction of membrane structure in both dry-casting and VIPS. Elimination of any partial diffusion coefficients lead to very different mass transfer paths and concentration profiles and predictions therefore of the solidified film structure.

References

[1] B. F. Barton, P. D. Graham, A. J. McHugh, Dynamics of spinodal decomposition in polymer solutions near a glass transition, Macromolecules, 31 (1998) 1672.

[2] B. F. Barton, A. J. McHugh, Kinetics of thermally induced phase separation in ternary polymer solutions. I. Modeling of phase separation dynamics, J. Polym. Sci. Part B: Polymer Physics, 37 (1999) 1449.

[3] B. F. Barton, P. D. Graham, A. J. McHugh, II. Modeling of phase separation dynamics, J. Polym. Sci. Part B: Polymer Physics, 37 (1999) 1461.

[4] C.S. Tsay, A.J. McHugh, Mass transfer modeling of asymmetric membrane formation by phase inversion, J. Polym. Sci. Part B: Polymer Physics, 28 (1990) 1327.

[5] S. S. Shojaie, W. B. Krantz, A. R. Greenberg, Dense polymer film and membrane formation via the dry-cast process. Part I. Model development, J. Membr. Sci. 94 (1994) 255.

[6] S. S. Shojaie, W. B. Krantz, A. R. Greenberg, Dense polymer film and membrane formation via the dry-cast process. Part II. Model validation and morphological studies, J. Membr. Sci. 94 (1994) 281.

[7] H. Matsuyama, M. Teramoto, T. Uesaka, Membrane formation and structure development by dry-cast process. J. Membr. Sci. 135 (1997) 271.

[8] H. Matsuyama, M. Nishiguchi, Y. Kitamura, Phase separation mechanism during membrane formation by dry-cast process, J. Appl. Polym. Sci. 77 (2000) 776.

[9] S. A. Altinkaya, B. Ozbas, Modeling of symmetric membrane formation by dry-casting method, J. Membr. Sci. 230 (2004) 71.

[10] S. A. Altinkaya, H. Yenal, B. Ozbas, Membrane formation by dry-cast process: model validation through morphological studies, J. Membr. Sci. 249 (2005) 163.

[11] H. Matsuyama, M.Teramoto, R. Nakatani, T. Maki, Membrane formation via phase separation induced by penetration of nonsolvent from vapor phase. I. Phase diagram and mass transfer process, J. Appl. Polym. Sci. 74 (1999) 159.

[12] H. Matsuyama, M.Teramoto, R. Nakatani, T. Maki, Membrane formation via phase separation induced by penetration of nonsolvent from vapor phase. II. Membrane morphology, J. Appl. Polym. Sci. 74 (1999) 171.

[13] H. C. Park, Y. P. Kim, H. Y. Kim, Y. S. Kang, Membrane formation by water vapor induced phase inversion, J. Membr. Sci. 156 (1999) 169.

[14] H. J. Lee, B. Jung, Y. S. Kang, H. Lee, Phase separation of polymer solution by nonsolvent vapor, J. Membr. Sci. 245 (2004) 103.
[15] H. Caquineau, P. Menut, A. Deratani, C. Dupuy, Influence of the relative humidity on film formation by vapor induced phase separation, J. Polym. Eng. Sci, 43 (2003) 798.

[16] W. Li, A. J. Ryan, I. K. Meier, Morphology development via reaction-induced phase separation in flexible polyurethane foam, Macromolecules 35 (2002) 5034.

[17] K. Matsuzaka, H. Jinnai, T. Koga, T. Hashimoto, Effect of oscillatory shear deformation on demixing processes of polymer blends, Macromolecules 30 (1997) 1146.

[18] J. R. DesNoyer, The role of phase inversion in the drug release kinetics of injectable polymer solutions, PhD thesis, University of Illinois, Urbana-Champaign, 2002.

[19] J.H. Kim, Y.S. Kang, Phase behavior and mechanism of membrane formation for polyimide /DMSO/water system, J. Membr. Sci. 187 (2001) 47.

[20] J. E. Anderson, R. Ulman, Mathematical analysis of factors influencing the skin thickness of asymmetric reverse osmosis membranes, J. Appl. Phys. 44 (1973) 4303.

[21] C. Castellari, S. Ottani, Preparation of reverse osmosis membranes. A numerical analysis of asymmetric membrane formation by solvent evaporation from cellulose acetate casting solutions, J. Membr. Sci. 9 (1981) 29.

[22] W. B. Krantz, R. J. Ray, R. L. Sani, K. J. Gleason, Theoretical study of the transport processes occurring during the evaporation step in asymmetric membrane casting, J. Membr. Sci. 29 (1986) 11.

[23] C.S. Tsay, A. J. McHugh, Mass transfer dynamics of the evaporation step in membrane formation by phase inversion, J. Membr. Sci. 64 (1991) 81.

[24] L. Yilmaz, A. J. McHugh, Analysis of nonsolvent-solvent-polymer phase diagrams and their relevance to membrane formation modeling, J. Appl. Polym. Sci. 31 (1986) 997.

[25] S. I. Sandler, Chemical and engineering thermodynamics, John Wiley and Sons, Inc., New York, 3rd edition, 1999.

[26] M. H. V. Mulder, C. A. Smolders, On the mechanism of separation of ethanol/water mixture by pervaporation: I Calculation of concentration profiles, Industrial and Engineering Chemistry Process Design and Development, 17 (1984) 289.

[27] C.S. Tsay, A.J. McHugh, A rationale for structure formation during phase inversion, J. Polym. Sci. Part B: Polymer Physics, 30 (1992) 309.

[28] S. Alsay, J.L. Duda, Modeling of multicomponent drying of polymer films, AIChE J. 45 (1999) 896.

[29] J. S. Vrentas, J. L. Duda, Predicting polymer/solvent diffusion coefficients using free-volume theory, AIChE J. 38 (1992) 405.

[30] J. M. Zelinski, J. L. Duda, Predicting polymer/solvent diffusion coefficients using free-volume theory, AIChE J. 38 (1992) 405.

[31] S. Hong, Prediction of polymer solvent diffusion behavior using free-volume theory, Ind. Eng. Chem Res. 34 (1995) 2536.

[32] D. Huang, G. B. McKenna, New insights into the fragility dilemma in liquids, J. Chem. Phys. 114 (2001) 5621.

[33] S. L. Simon, D. J. Plazek, J. W. Sobieski, E. T. McGregor, Physical aging of a polyetherimide: volume recovery and its comparison to creep and enthalpy measurements, J. Polym. Sci. Part B: Polymer Physics, 35 (1997) 929.

[34] C. Raman, Modeling drug release from fast phase inverting injectable drug delivery systems, MS thesis, University of Illinois, Urbana, 2002.

[35] J. Y. Kim, H. K. Lee, K. J. Baik, S. C. Kim, Liquid-liquid phase separation in polysulfone/solvent/water systems, J. Appl. Polym. Sci. 65 (1997) 2643.

[36] T. Yong, C. Tao, P. Lai, Phase behavior of polyetherimide in mixtures of N-methyl-2-pyrrolidinone and methylene chloride, J. Polym. 44 (2003) 1689.

[37] G. R. Fernandes, J. C. Pinto, R. Nobrega, Modeling and simulation of the phase-inversion process during membrane preparation, J. Appl. Polym. Sci. 82 (2001) 3036.

[38] W. H. McAdams, Heat transmissions, third ed., McGraw-Hill, New York, 1954.

[39] F. P. Incropera, D. P. Dewitt, Fundamentals of heat and mass transfer, Wiley, New York, 1990.

[40] T. Boublik, V. Fried, E. Hala, The vapor pressure of pure substances: seclected values of the temperature dependence of the vapor pressures in the normal and low pressure region, 2nd ed., Elsevier, New York, 1984.

[41] S. H. Lee, Y. C. Bae, Thermal stress analysis for polyimide thin film: the effect of solvent evaporation, Macromol. Theory Simul. 9 (2000) 281.

[42] C.S. Tsay, A.J. McHugh, An improved numerical algorithm for ternary diffusion with a moving interface, Chem. Eng. Sci. 46 (1991) 1179.

[43] H. Sundqvist, G. Veronis, A simple finite-difference grid with nonconstant intervals, Tellus, 22 (1970) 26.

[44] S. Alsoy, Modeling of polymer drying and devolatilization processes, PhD thesis, The Pennsylvania State University, University Park, 1998.

Vita

Yuen-Lai Yip was born on December 21, 1980 in Hong Kong to Yuk-Ying and Kin-Lau Yip. She received her elementary and high school education in Hong Kong. She immigrated to U.S. with her family in 1999, and attended Polytechnic University in Brooklyn, New York. While studying at Polytechnic, she was awarded Polytechnic Promise Scholarship, Who's Who Among Students Award, USAA National Collegiate Engineering Award and Omega Chi Epsilon Award. She graduated in June 2003 with a B.S. degree in chemical engineering (cum laude). In August of 2003, Yuen-Lai joined Lehigh University's chemical engineering department at Bethlehem, Pennsylvania and she was awarded Byllesby Fellowship.

END OF TITLE